

Universitat Autònoma de Barcelona
Institut de Ciència de Materials de Barcelona (ICMAB-CSIC)
Nanopto

On Improving the Efficiency of Organic Photovoltaic Devices: Novel Strategies

Martí Gibert Roca

Under the supervision and tutoring of:

Mariano Campoy Quiles

Submitted in part fulfilment of the requirements
for the degree of Doctor of Philosophy in Materials Science
of the Universitat Autònoma de Barcelona, February 2022

Contents

Chapter 1: Enhancing OPV Performance with Nanoimprinted 2D Photonic Structures 1

1.1	State of the Art	2
1.2	Materials and Methods	4
1.3	Nanostructured Solar Cells	7
1.3.1	Introduction	7
1.3.2	Materials and Methods	9
1.3.3	Results and Discussion	10
1.4	Nanostructured NIR Photodetectors	15
1.4.1	Introduction	15
1.4.2	Device Fabrication	19
1.5	Nanostructure Electrical Optimization	25
1.5.1	Device Characterization	27
1.5.2	NIR Multiwavelength Photodetector	38
1.6	Conclusions	41

Appendices

1.A	Nanostructure Electrical Optimization	43
1.A.1	Active layer Thickness	47
1.A.2	Annealing	50
	Bibliography	52

List of Tables

1.1 JV curve extracted values for nanostructured and flat P3HT:PC61BM based
organic solar cells. 11

List of Figures

1.1	Layer stack configuration for nanostructured OPV devices seen upside down with the silver back electrode on top. Figure adapted from: J. Mater. Chem. C, 2020, 8, 9688 ¹	5
1.2	a) Soft nanoimprinting lithography process steps illustration. b) Crossection SEM image from a finished nanostructured OPV device. c) Picture of a finished nanostructured device showing different iridescence colours for each nanostructure; L600, L500, L400 from top to bottom. Figure adapted from: J. Mater. Chem. C, 2020, 8, 9688 ¹	6
1.3	(a) Integrating sphere extinction (1-R-T) measurements of inverted (left) and conventional (right) architectures for both nanostructured and flat solar cells. (b) FDTD simulation of the absorption spectrum for a nanostructured and flat P3HT:PC61BM based inverted solar cell with a nanostructure lattice parameter of 400 nm and a thickness of 130 nm, with separate active layer contribution. (c) Incoupled light escaping through the device edge while being measured on the integrating sphere.	12
1.4	JV Curves from nanostructured and flat cells based on a P3HT:PC61BM active layer blend with two different nanostructure lattice parameters.	12

1.5	(left) JV curve of three PBDBT:ITIC based organic solar cells, a flat pristine reference a DIO containing flat reference and a DIO containing nanostructured solar cell. (right) Crystallite formation promoted by DIO presence on PBDBT:ITIC based solar cells for a pristine region and a region that has been under pressure in contact with a PDMS stamp that has undergone partial recrystallization. . . .	13
1.6	EQE spectra of P3HT:PC61BM based nanostructured and flat solar cells with efficiency oscillations along the absorption tail, in the NIR region, present only in the nanostructured cells.	15
1.7	Schematic visualization of the band structure and the charge transfer state within the band diagram of a generic type II donor acceptor blend, with a staggered gap configuration.	17
1.8	Cross-section SEM image of a nanostructured photodetector with all the conforming layers colorized for better visualization. The lowermost ITO layer is missing because the image was taken in a ITO free area of the patterned substrate.	21
1.9	Dispersion relation of the wavelength vs parallel wavevector of the incident light for a) P3HT:PC61BM and b) PBTTT:PC71BM blends. The first diffraction orders of the photonic crystal arrays with lattice parameters of 400, 500 and 600 nm (blue dashed lines) grants to the incident light the necessary momentum to couple to the guided modes within the semiconductor material in the CTS range of absorption (a) red and b) purple lines). Figure adapted from: J. Mater. Chem. C, 2020, 8, 9688 ¹	23

- 1.10 (a) Calculated absorption of the fabricated devices with fully coherent light (grey dashed) and 150 micron coherent light (red). (b) External quantum efficiency measurements for a PBTTT:PC71BM nanostructured photodetector with a lattice parameter of $L = 500$ nm. Sample scheme for nanostructured and flat devices (c), (d) and calculated electric fields at wavelengths 862 and 907 nm (e), (f) and (g), (h). Figure adapted from: J. Mater. Chem. C, 2020, 8, 9688¹ 24
- 1.11 FTIR absorption spectra of PBTTT:PC71BM based devices for various nanostructure lattice parameters as well as flat reference (left). Picture of a finished device exhibiting different iridescence characteristics for different photonic crystal lattice parameters. From top to bottom: $L = 400$, $L = 500$ and $L = 600$ nm (right). 28
- 1.12 External quantum efficiency measurements for non-structured (flat) and differently nanostructured photodetectors ($L400$, $L500$ and $L600$) with an active layer of P3HT:PC61BM (left), PBTTT:PC71BM (right). Figure adapted from: J. Mater. Chem. C, 2020, 8, 9688¹ 29
- 1.13 Ratio between nanostructured and flat EQE curves (Enhancement Factor) for three different lattice parameters and two different active layer materials; P3HT:PC61BM (left), PBTTT:PC71BM (right). 30
- 1.14 EQE measurements with various reverse applied V bias from 0 V to 23 V for (top) nanostructured and (bottom) non-structured (flat) PBTTT:PC71BM photodetectors. Figure adapted from: J. Mater. Chem. C, 2020, 8, 9688¹ 32
- 1.15 Responsivity of PBTTT:PC71BM photodetectors at different wavelengths for both nanostructured and flat devices at zero V bias (left). Responsivity at 907 nm for different V bias of $L = 500$ (nanostructured) and non-structured (flat) PBTTT:PC71BM photodetector (right). Figure adapted from: J. Mater. Chem. C, 2020, 8, 9688¹ 33

1.16	Dark current of both flat and $L = 500$ nanostructured devices at various reverse V bias. Figure adapted from: J. Mater. Chem. C, 2020, 8, 9688 ¹	34
1.17	On/Off ratio of flat (dashed line) and L500 PBTTT:PC71BM based nanostructured devices at different wavelengths for various reverse V bias voltages from 1 V (red) to 23 V (green). Figure adapted from: J. Mater. Chem. C, 2020, 8, 9688 ¹	35
1.18	Time dependent normalized photoresponse measurement for both flat and $L = 500$ PBTTT:PC71BM based nanostructured devices at 0 V bias. Figure adapted from: J. Mater. Chem. C, 2020, 8, 9688 ¹	36
1.19	Measured linear dynamic range of L500 PBTTT:PC71BM nanostructured photodetector at 0 V bias. Figure adapted from: J. Mater. Chem. C, 2020, 8, 9688 ¹	37
1.20	Light beam induced photocurrent (LBIC) maps of a large area continuous back electrode photodetector, at 3 different excitation wavelengths: (a) 710 nm, (b) 941 nm and (c) 1032 nm, with 3 different nanostructured zones. From top to bottom: $L = 400$, $L = 500$ and $L = 600$ nm. Figure adapted from: J. Mater. Chem. C, 2020, 8, 9688 ¹	39
1.21	EQE enhancement peaks for a P3HT:PC61BM photodetector with a Schottky barrier formed between the active layer and the gold back electrode (right). Schottky barrier formation schematic diagram for metals with different work-functions (left).	45
1.22	Dark Current Density plot for various nanostructuration depths and flat reference for comparison.	45

1.23	EQE curves for P3HT:PC61BM photodetectors with various MoO ₃ (HTL) thicknesses for flat photodetectors, on the left, as well as nanostructured photodetectors, on the right, with a zoomed region.	46
1.24	Dark Current Density plot for two different HTL thicknesses in nanostructured and flat photodetectors for both P3HT:PC61BM based devices (left) and PBTTT:PC71BM based devices (right).	47
1.25	Light absorption profile across the active layer of a thick photodetector for various light wavelengths. Figure inspired by Armin et al. ²	48
1.26	Dark Current Density plot for two different active layer thicknesses in nanostructured and flat photodetectors for both P3HT:PC61BM based devices (left) and PBTTT:PC71BM based devices (right).	49
1.27	EQE response of L500 P3HT:PC61BM (left) and PBTTT:PC71BM (right) photodetector for different active layer thicknesses with zoomed region	50
1.28	EQE response of L500 P3HT:PC61BM (left) and PBTTT:PC71BM (right) photodetector for different active layer annealing conditions.	52

Chapter 1

Enhancing OPV Performance with Nanoimprinted 2D Photonic Structures

Abstract

In this chapter we will explore how controlled nanostructuration of organic solar cells and organic photodetectors, more specifically active layer and back electrode nanostructuration, can modify their spectral response as well as their overall performance. The results of this chapter are an expansion of the work published in J. Mater. Chem. C, 2020, 8, 9688.¹

~~In this chapter,~~ we have manufactured organic solar cells and organic photodetectors, and nanostructured their active layers in the shape of a 2D photonic crystal, consisting of a square array of cylindrical holes, in order to increase their absorption and overall efficiency. These devices have been mainly developed using P3HT:PC61BM, PBTTT:PC71BM and PBDBT:ITIC as photoactive materials. Along this process, several characteristics of the photonic architecture, like the feature depth or the lattice parameter, have been modified in order to guarantee basic device performance as well as to enhance and tune its spectral response. In the particular case of the photodetectors, we have tuned the photonic crystal properties to enhance their NIR response by enhancing the charge transfer state absorption. A variety of characterization techniques have been used to analyze our devices in order to get a good picture of their performance.

May need 2 define all those in abbrev. section.

Need to integrate?

We have manufactured both nanostructured and flat devices, under the same conditions, for a fair performance comparison on each of the samples.

1.1 State of the Art

As we have discussed in (??: ??), the active layer thickness of most OPV devices is limited by the short exciton diffusion length, arising from the low charge mobility inherent to organic semiconductors.³⁻⁵ This thickness limitation, ^{on the order of 100 nm,} ultimately limits the maximum absorption of the active layer, lowering the theoretical maximum PCE that OPV devices could achieve.^{6,7} This problem has been addressed from several perspectives, from enhanced charge extraction layers^{8,9} and higher charge mobility active materials^{10,11} all the way to ferroelectric polarization of the active layer,¹²⁻¹⁴ in order to increase charge collection probability on the electrodes. Nevertheless, one of the most attractive ~~is to utilize some form of light trapping to enhance active layer absorption from an optically oriented perspective.~~⁷

Light management has emerged as an important field to help with this trade-off, which has been limiting organic photovoltaic performance,^{4,15} to enhance light absorption within OPV devices without compromising charge extraction. By incorporating photonic structures, the optical path length and the electromagnetic field strength can be tuned, thus enabling an increase in the total effective absorption without increasing the active layer thickness.⁷ These light management techniques have been successfully used, both in organic solar cells and organic photodetectors, to enhance their performance either on a specific wavelength range or throughout the entire spectrum.^{16,17}

There are several approaches that fall into the light management umbrella. On one hand, there are those that exploit the conventional ray optics strategies that are mainly based on reflection

Flat is a "strong" word... atomically flat? maybe "bare"?

ojo!

strategies?

and refraction such as: anti-reflection coatings,^{18,19} collector mirrors,²⁰ v-folded substrates,^{21–23} fiber based shape photovoltaics^{24,25} and micro lenses,^{26,27} which exploit light trapping up to the classical limit. These approaches ease the incoupling of light into the solar cell and extend the path of the photons within the active layer, leading to a much longer interaction distance that gives the photon a higher chance of being absorbed. However, when using conventional light trapping the absorption enhancement is limited to $4n^2$, where n is the refractive index of the active layer.^{28,29} In order to bypass this limitation, the scientific community has been putting more and more effort on approaches based on wave nature of light, such as microcavities,^{30,31} optical spacers,³² distributed Bragg reflectors,³³ photonic crystals,^{16,18,32–36} quasi-periodic³⁷ or disordered nano-patterns,³⁸ nanoparticles (NPs),^{39,40} and plasmonic nanostructures.^{3,40–42} These strategies usually rely on some kind of nanostructure that can be tuned to manipulate light in order to increase absorption within the active layer of OPV devices, boosting the enhancement factor limit by an order of magnitude, up to $12 \times 4n^2$.^{43,44} Not only that, but these nanostructures provide us with the ability to tune the absorption's spectral response, providing a whole new set of tools for selective wavelength enhancement,^{45,46} which can be ~~really~~ useful in the world of PV to be used, for example, in photodetectors or tandem solar cells. That is why the scientific community has started to implement such light management (techniques) on emerging PV fields such as OPV,^{36,47,48} dye sensitized solar cells^{33,49–52} or perovskites.⁵³ These structures are so promising that even well established PV fields, like silicon based photovoltaics, have some amount of literature reporting on them.^{16,35,54,55}

In this work, we will mainly focus on the role of photonic crystal nanostructures in organic solar cells and organic photodetectors. We have chosen to use active layer nanostructuring as our light trapping mechanism because it is one of the most reliable and scalable processes available, especially when using roll-to-roll compatible techniques such as the ones utilized in this thesis.^{56,57} Besides, by nanostructuring the active layer, we can deposit thin active layers that absorb light efficiently, using less photoactive material, while adding just one step to the manufacturing process, without significantly increasing its complexity and ~~material~~ cost.^{58,59}

To study the effect of these nanostructures on OPV, we have modified the active layer and the back electrode of an organic solar cell into a photonic crystal as a light trapping mechanism. Along the process, we have explored the advantages and difficulties that arise when trying to implement such 2D nanostructures on the active layer and the back electrode of OPV devices. This photonic nanostructure consists of a 2D periodic structure that in couples the incoming light into the active layer, enhancing the optical path and increasing the electric field strength, thus rendering higher absorption efficiencies within the photoactive material.

It is worth noting that even though we talk about photodetectors in general, within all different types of photodetectors, our work is focused on organic photodiodes.

1.2 Materials and Methods

Most of the materials and methods used in this chapter are common throughout the various different types of devices manufactured. However, methods specific to a certain device will be explained in detail in their own subsection.

As one of the main active layer materials we have decided to use P3HT:PC61BM, because, since it has one of the lowest synthetic complexity of all photoactive polymers, it is really inexpensive, thus being widely available, and on top of that it is the most studied and well understood material blend in the world of OPV.^{60–64} Besides P3HT:PC61BM, we have used a variety of other active materials in our solar cells and organic photodetectors, which are further described and explained in their own subsections.

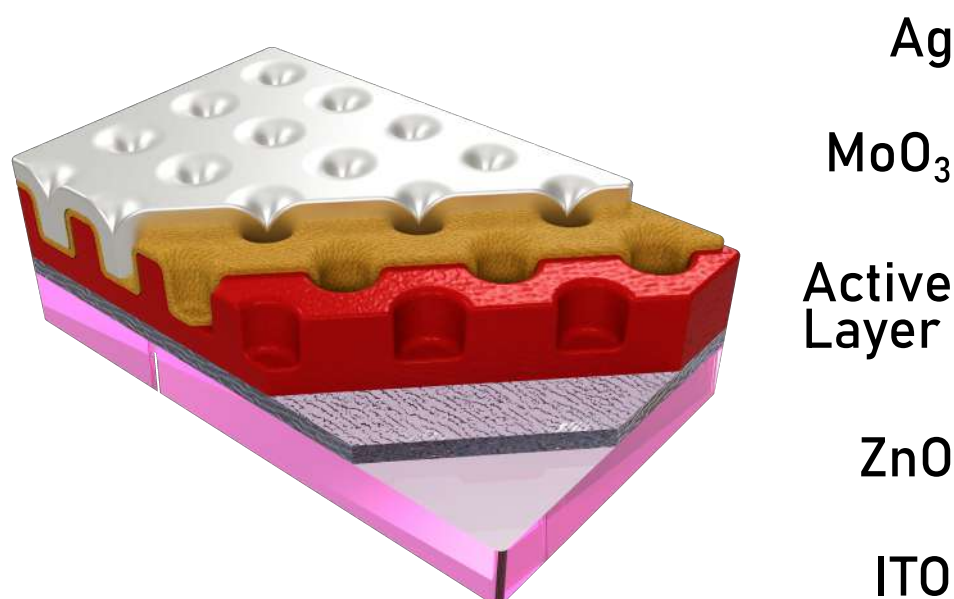


Figure 1.1: Layer stack configuration for nanostructured OPV devices seen upside down with the silver back electrode on top. Figure adapted from: J. Mater. Chem. C, 2020, 8, 9688¹

In figure 1.1 we can see a complete schematic view of the different layers that compose both our solar cells and our photodetectors. Their main differentiating characteristics, are their specific photoactive material and their active layer thickness.

The lowermost layer, after the ITO substrate, is the electron transport layer (ETL), which we deposit from a ZnO nanoparticle solution on an ITO covered glass substrate by blade coating, a technique often used as a pre-upscaling method.⁵⁶⁻⁵⁹ After annealing the ZnO film to remove the solvent and settle the structure, we deposit a layer of photoactive material using same technique. At this point, we nanostructure the active layer by using a variety of techniques that differ depending on the active layer material and the type of device. They are further specified below and through the chapter for specific conditions.

On top of the nanostructured active layer, a 10 nm thick MoO₃ layer is deposited by thermal evaporation. The thickness was set so that it was enough to have a uniform film, without any pinholes and good charge blocking characteristics while maintaining the diffractive behaviour of

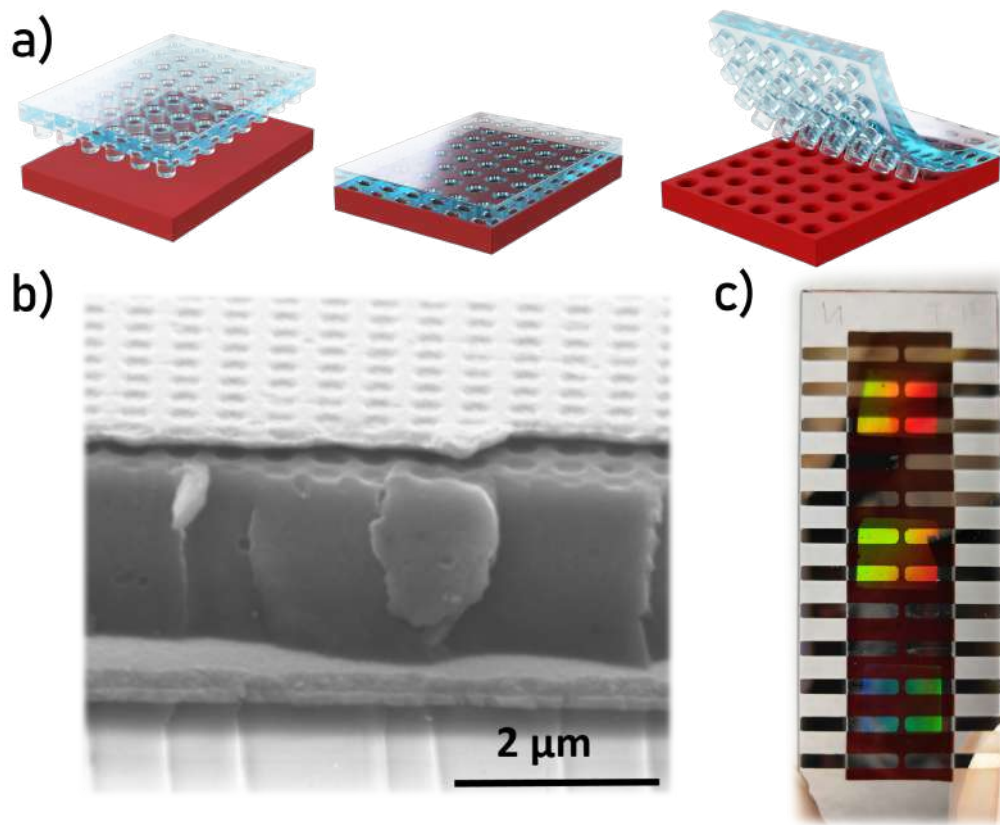


Figure 1.2: a) Soft nanoimprinting lithography process steps illustration. b) Cross-section SEM image from a finished nanostructured OPV device. c) Picture of a finished nanostructured device showing different iridescence colours for each nanostructuration; L600, L500, L400 from top to bottom. Figure adapted from: J. Mater. Chem. C, 2020, 8, 9688¹

the photonic crystal. As the last layer, we deposited a thick 200 nm Ag back electrode contact, also by thermal evaporation. The back electrode, being deposited onto the nanostructured active layer, adopted the shape of the nanostructure which provided the sample with a strong optical response.

Finally, most devices are encapsulated with UV curable epoxy resin and a glass coverslip to slow down oxygen and moisture driven degradation.

To fabricate these photonic structures, we have used a technique called thermal nanoimprinting lithography. The nanostructure is formed on the active layer by heating it above its glass

Ref?

transition temperature, placing a hybrid PDMS stamp onto the polymer blend, and applying a pressure of up to 5 bar. The combination of the pressure with the partial liquefaction of the polymer blend, force the active layer to take the shape of the hard stamp. After cooling it down below its glass transition temperature and removing the pressure, the PDMS stamp can be carefully removed, revealing a nanostructured active layer (figure 1.2 a)). When the HTL and the back electrode are subsequently deposited on top of the nanostructured active layer, they both take its shape (figure 1.2 b)), resulting in a nanostructured layer stack, which will act both as a reflecting and diffracting element. The diffraction characteristics are easily visible with the naked eye in the form of a beautiful iridescence, as we can see in figure 1.2 c)). These nanostructures were performed with stamps with different feature depths, as we will see in the later sections, because of several electrically related problems.

The nanostructured stamps used during the nanostructuration process were fabricated in collaboration with Dr. Molet, with the methodology described in *??: ??*. These stamps produced nanostructures consisting on a square lattice of cylindrical holes, evenly spaced on the xy plane as seen in figure 1.2. These holes had varying depth and lattice constants so as to explore the effect of these parameters in our devices.

1.3 Nanostructured Solar Cells

1.3.1 Introduction

Increasing the amount of light a solar cell can absorb, and therefore convert into electrical power, is a neat strategy to increase their efficiency. That is why light management techniques have been employed in almost every existing photovoltaic technology.^{16, 33, 47, 51, 53, 55, 65} Technologies that use thick active layers ($\sim > 1 - 10\mu\text{m}$), where reflected light is the biggest concern,

focus on approaches such as anti-reflection coatings, since light is completely absorbed within the thick active layer.⁶⁶⁻⁶⁸

On the other hand, thin film technologies, such as OPV, use different light management approaches to increase the absorption within the thin active layer, such as plasmonics or photonics,^{41,47,51} which tend to rely to some degree on the partial nanostructuring of the device.⁷ These nanostructures do not only provide light trapping capabilities, but can increase the surface area to volume ratio and reduce solar cell thickness, therefore using less material overall.^{69,70} Besides, they have the potential to reduce the distance between charge carriers and the p-n junction, or the donor-acceptor interface, facilitating charge collection.⁵

Despite the potential efficiency increase of nanostructured solar cells, and their rapid development, device performance has not been significantly raised, mainly due to hindered electrical properties related to the nanostructuring process.⁷ With the exception of anti-reflection coating nanostructures that, by being outside ~~the~~ the solar cell, have little to no detrimental effect on its electrical characteristics.¹⁸

In the world of OPV, however, short charge diffusion lengths encourage scientists to keep on trying to use photon management techniques to overcome the limited absorption provided by such thin layers. This is usually achieved by implementing some kind of nanostructure inside the solar cell, which provides light trapping and/or field enhancement capabilities. Nevertheless, these strategies tend to rely on techniques that are not always easily scalable, like most techniques used in nanofabrication, and are sensitive to manufacturing errors.⁷

In this work, we have implemented soft nanoimprinting lithography, a roll-to-roll compatible nanostructuring technique,⁵⁶⁻⁵⁹ to nanostructure the active layer of organic solar cells to increase their light trapping capabilities. By nanostructuring the active layer we provide

a template on which the metallic back electrode is deposited, resulting on a nanostructured active layer and back electrode. This nanostructured stack has the shape of a photonic crystal, which, by incoupling incoming sunlight, increases the overall absorption, and in theory the final efficiency of the solar cell. This layer stack is especially powerful because the optical contrast between metals and organic polymers is really high, enhancing the cell's light trapping capabilities.⁴⁴

1.3.2 Materials and Methods

The nanostructured organic solar cells were manufactured with an active layer based on P3HT:PC61BM, as explained in section ??: ??. Since devices were manufactured both in inverse and conventional architectures, four different transport layers were used: PEDOT:PSS and MoO₃ as hole transport layers, and ZnO NP and Ca as electron transport layers. However, seeing that only inverse architecture devices provided useful electrical results, device electrical characterization is focused on the inverted architecture.

In order to study the effect of nanostructuring on higher efficiency materials, we used PB-DBT:ITIC as photoactive material, which was one of the highest performing materials at the time of the experiments.⁷¹ This particular active layer blend was used in an inverted configuration, and it required the use of DIO to act as a plasticiser for the nanostructuration step.

Two main techniques were used for the nanostructuring of the active layer. The first one was solvent assisted nanoimprinting lithography in which we take advantage of the fact that, when the active layer is not completely dry, we can place a nanostructured stamp on top, and the active layer will take the shape of the nanostructure as the solvent evaporates. This nanostructuring technique provided great results for P3HT:PC61BM based active layer blends, but

it did not provide good results with PBDBT:ITIC based active layers. In the latter, the active layer processing characteristics and drying times completely obstructed the application of this technique.

In order to nanostructure PBDBT:ITIC active layers, we decided to use thermal nanoimprinting lithography, a technique that proved to be much more reliable in the long run.

For this particular study, a wide variety of nanostructure lattice parameters were chosen, ranging from 400 nm all the way up to 800 nm. However, since, at first we saw no significant differences in the general light trapping capabilities between different nanostructure pitches on the visible range, we decided to prioritize other aspects of the study.

1.3.3 Results and Discussion

Before manufacturing devices, we decided to simulate the possible absorption increase that a nanostructure would provide to a basic P3HT:PC61BM solar cell. For that, Dr. Molet performed some simple FDTD simulations, which provided some promising results. As we can see in figure 1.3 b), there is a theoretical absorption increase in almost the entire visible and NIR range, for a nanostructured P3HT:PC61BM based solar cell with a nanostructure lattice parameter of 400 nm and a thickness of 130 nm. We can see in that same figure that a part of the absorption enhancement is directly attributed to an increased absorption within the P3HT:PC61BM active layer.

In order to assess the light-trapping capabilities of our solar cells, we manufactured and measured the absorption of complete devices by using an integrating sphere. As we can see in the extinction (1-R-T) graphs (figure 1.3), the main extinction gains are located below the band

gap of the active layer blend for both the inverted and conventional architectures. Sub-panel a), on the left, shows a P3HT:PC61BM based inverted solar cell that exhibits great absorption gains, especially on the NIR region. However, upon further inspection, we see that the absorption enhancement in our active layer is much more modest, ~~as~~ ^{compared} ^{to} ^{the} ^{one} ^{...} as predicted by our simulations. On the right panel, we see a similar behaviour, however, since this sample did not have any active layer region without back electrode, we could not measure the active layer contribution to the total absorption. As we will see in later sections, this effective absorption increase is more related to the incoupling of guided modes, which do not necessarily lead to complete light absorption within the active layer. We can get an early hint of this phenomenon from the red light that comes out of the side of our solar cell, indicating that a significant fraction of that incoupled light is not getting efficiently absorbed (figure 1.3 c)).

As we can see in figure 1.4, the nanostructured solar cells exhibited a somewhat enhanced J_{sc} , which is well correlated with the increase in light absorption. This enhancement however, was not as high as the increase in absorption might have suggested. This can be attributed to the fact that most of the absorption enhancement occurred well below the band gap of the solar cells, and the active layer contribution to that absorption increase was moderate. This fact combined with a lower fill factor, probably due to higher recombination caused by surface defect traps,⁷² led to more or less equivalent efficiencies for both nanostructured and flat solar cells (table 1.1).

	Voc (V)	Jsc (mA)	FF (%)	Efficiency (%)	Rs (Ω)	Rsh (k Ω)
Nanostructured	0.6 \pm 0.02	-8.4 \pm 0.2	42 \pm 6	2.12 \pm 0.2	140 \pm 60	13 \pm 5
Flat	0.6 \pm 0.01	-7.6 \pm 0.4	47 \pm 8	2.14 \pm 0.1	100 \pm 20	21 \pm 2

Table 1.1: JV curve extracted values for nanostructured and flat P3HT:PC61BM based organic solar cells.

We also decided to try the nanostructuring process on a high efficiency material blend based on a NFA, PBDBT:ITIC. However, due to its crystalline structure properties,⁷³ this active layer blend could not be easily nanostructured neither by solvent assisted nanoimprinting lithogra-

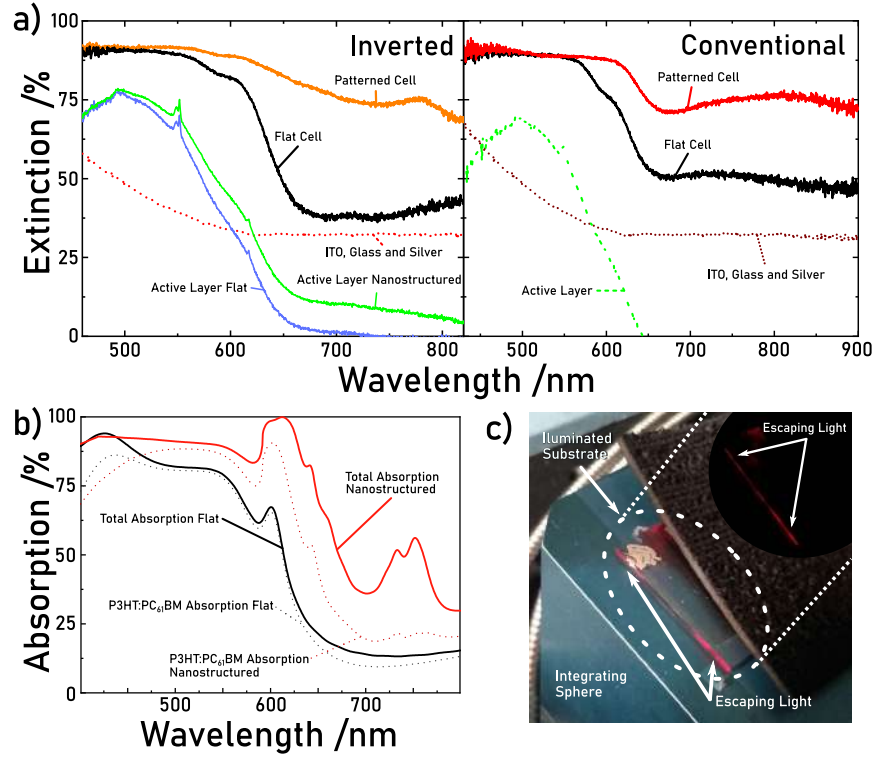


Figure 1.3: (a) Integrating sphere extinction (1-R-T) measurements of inverted (left) and conventional (right) architectures for both nanostructured and flat solar cells. (b) FDTD simulation of the absorption spectrum for a nanostructured and flat P3HT:PC₆₁BM based inverted solar cell with a nanostructure lattice parameter of 400 nm and a thickness of 130 nm, with separate active layer contribution. (c) Incoupled light escaping through the device edge while being measured on the integrating sphere.

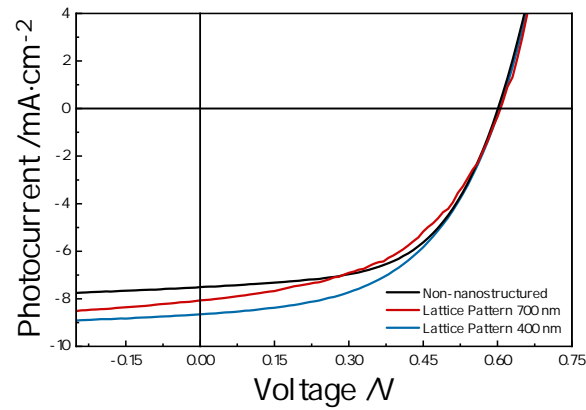


Figure 1.4: JV Curves from nanostructured and flat cells based on a P3HT:PC₆₁BM active layer blend with two different nanostructure lattice parameters.

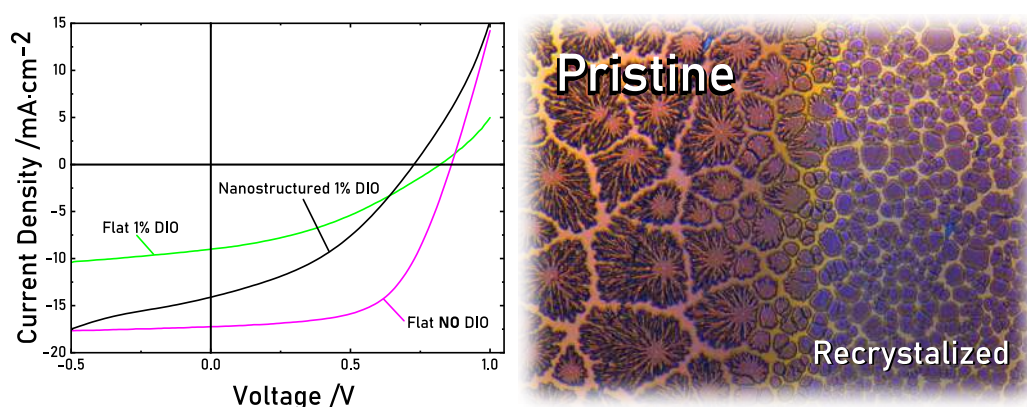


Figure 1.5: (left) JV curve of three PBDBT:ITIC based organic solar cells, a flat pristine reference a DIO containing flat reference and a DIO containing nanostructured solar cell. (right) Crystallite formation promoted by DIO presence on PBDBT:ITIC based solar cells for a pristine region and a region that has been under pressure in contact with a PDMS stamp that has undergone partial recrystallization.

phy nor by thermal nanoimprinting lithography. We attempted to nanostructure PBDBT:ITIC based active layers under a pressure of up to 6 bar and a temperature of up to 200°C without success. That is why we decided to add DIO, a commonly used additive, in a 1% concentration to temporally act as a plasticiser, so that the active layer could be nanostructured while trying to minimize detrimental effects on the photoactive material.

With DIO and thermal nanoimprinting lithography, we were able to nanostructure the active layer of PBDBT:ITIC based solar cells. Nonetheless, this came at a high price, since, as we can see in figure 1.5 (left), while the electrical performance of a pristine PBDBT:ITIC based device is in agreement with previously published data, when DIO is added, its performance is severely hindered. The nanostructuration process seems to revert these effects to a certain degree, by increasing the J_{sc} and slightly reducing the fill factor when compared to a flat device with DIO, in a similar fashion as the behaviour we observed with P3HT:PC61BM based solar cell. However, for PBDBT:ITIC active layers with DIO, both nanostructured and flat devices perform significantly lower than any of the flat pristine samples, rendering the process counterproductive.

Volume
or
mass
(V or m)
2.2
 $\frac{m}{V}$
2

We attribute this drop in performance to a strong phase separation made possible by the presence of DIO, which can act as a solvent.⁷⁴ As we see in figure 1.5 (right), big crystals have developed all along the surface of the active layer, which are less present around the regions that were in contact with the PDMS stamp during NIL. These crystallites form immediately after blade coating the active layer, and they seem to be temperature sensitive, since we see that after nanostructuring the active layer with thermal nanoimprinting lithography, the areas that have been under pressure at high temperatures, exhibit smaller crystallite size than those which were not under pressure. This could be related to pressure dependent phase separation, and could partially explain the higher performance of these particular nanostructured solar cells.

→ this is difficult to parse ...
consider breaking down in shorter sentences.

Parallely, we performed EQE measurements on our solar cells to verify the spectral regions in which light-trapping was providing an enhanced electrical response. We can see in figure 1.6 that, while our P3HT:PC61BM solar cells exhibit some general enhancement in the visible region, they show interesting peaks around the NIR well below the band gap of the photoactive material. These peaks were not present in the non-nanostructured solar cells, so they must have been a result of the nanostructured active layer and back electrode stack. Besides, they seem to be dependent on the nanostructure pitch, as they are clearly and consistently different for the different lattice parameters.

The fact that we did not manage to increase the overall efficiency of organic solar cells with photonic crystals, combined with these interesting peaks that appeared below the band gap absorption of our material, made us change course, and focus into studying this phenomenon more in depth, which leads us to the next section; Nanostructured NIR Photodetectors.

→ my own?

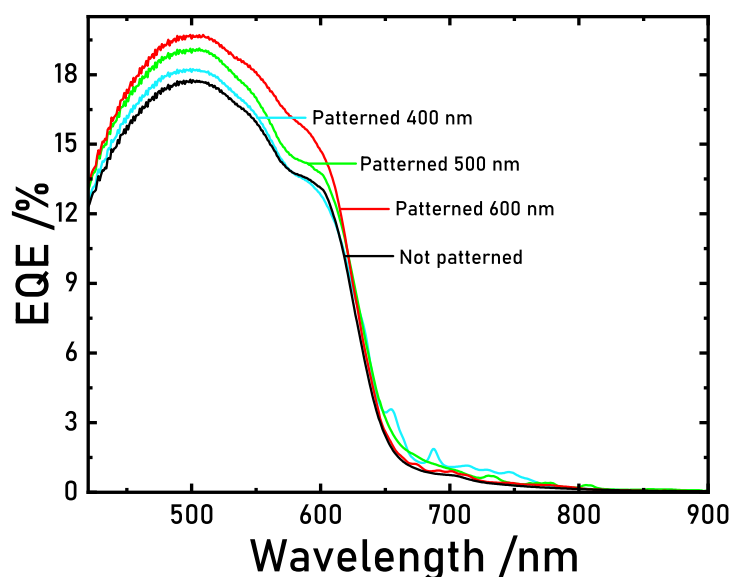


Figure 1.6: EQE spectra of P3HT:PC61BM based nanostructured and flat solar cells with efficiency oscillations along the absorption tail, in the NIR region, present only in the nanostructured cells.

1.4 Nanostructured NIR Photodetectors

1.4.1 Introduction

In our technologically-oriented society, near infrared (NIR) photodetectors can be found everywhere, since we rely on them on a daily basis in applications such as automatic sliding doors, NIR cameras, remote controls, telecommunications, spectrophotometers, and devices for medical diagnosis.^{75,76} Currently, NIR photodetector technologies are based on the combination of regular silicon or, to a lesser extent, III-V (InGaAs) photodetectors with colour filters or gratings.^{77,78} However functional and reliable, such wafer-based approaches, fail to satisfy the new demands for wearable, cheap and flexible devices. That is why appealing alternatives are emerging such as organic photodetectors (OPDs), which are flexible, have low embedded energy processing and are highly compatible with available and easily scalable techniques like roll-to-roll processing.⁵⁶⁻⁵⁹ On top of that, the composition of organic polymers and/or small organic molecules, can be chemically tuned to provide a variety of absorption ranges, further increasing the appeal of organic photodetectors.⁷⁹⁻⁸¹

Chemical tailoring of organic molecules has worked well within the visible range, however extending OPD wavelength response towards the NIR range while maintaining device performance still remains ~~quite~~ a challenge.⁸² Organic synthetic chemists are continuously developing new polymers and small molecules, with ever smaller band-gaps that go deeper into the infrared region.^{83,84} Nevertheless, manufacturing these exotic materials is a resource-intensive process, that requires great effort and costs a significant amount of money, reducing their potential to be used in real devices.⁸³ Furthermore, each new material is usually optimized for a specific wavelength range, which means that large number of new molecules have to be synthesized to operate along the solar spectrum.⁸⁵

Parallely, a different branch of research has been trying to extend and increase OPD response on the NIR region by using inexpensive, readily available organic semiconductors. Instead of focusing on tuning the intrinsic absorption of the material itself, this research has focused on alternative strategies to increase OPD response within the NIR region.^{86,87} One simple yet powerful approach consists in taking advantage of the filtering effect in thick polymer layers, also known as charge collection narrowing.² With this effect we can obtain narrow peaks with high external quantum efficiencies in the NIR region. There is, however, a downside to this approach; since it relies on the intrinsic absorption of the active layer materials, it still requires low band-gap molecules to go deeper into the NIR.⁸⁸⁻⁹⁰

Another elegant alternative consists in taking advantage of the direct intermolecular charge transfer state (CTS) absorption, to extend the OPD wavelength response far into the NIR region without the need of any low band-gap material.⁹¹ The CTS is the state that results from the interaction between the highest occupied molecular orbital (HOMO) of the donor and the lowest unoccupied molecular orbital (LUMO) of the acceptor. This state is only present at the donor-acceptor interface, where the electronic orbitals with different energies come together to

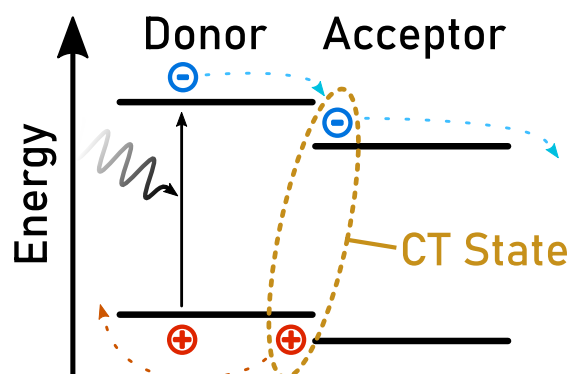


Figure 1.7: Schematic visualization of the band structure and the charge transfer state within the band diagram of a generic type II donor acceptor blend, with a staggered gap configuration.

form a new, intermediate state. This newly created state usually exhibits a lower transition energy than its composing states for a type II hetero-junction, such as those found in typical donor/acceptor blends. To put it simply, the energy levels form a staggered step-like shape, like the one that can be seen in figure 1.7. The lower transition energy of the CTS, endows the blend with the possibility to absorb light with longer wavelengths than each of its separate components, with a broad band absorption spectrum.

Because it is mainly localized within the donor acceptor interface CTS absorption strength is strongly dependant on molecular intermixing.⁹² Unfortunately, CTS absorption strength is around two orders of magnitude lower than singlet absorption strength due to the fact that it is an intermolecular state.⁸⁴ This intrinsically low oscillator strength often demands for the use of very thick active layers, at high reverse voltages, in order to guarantee light absorption and efficiently extract the generated charges.⁹³ For traditional device architectures, in order to increase the absorption of the CTS, active layer thicknesses must be increased enormously (up to tenths of microns). This requires applying biases of up to hundreds of volts to extract charges efficiently.⁹³ Aiming to avoid such high voltages and thick layers, research has focused on light trapping schemes in search for an interesting alternative to greatly enhance CTS absorption.

A recent development in the field of CTS absorption enhancement is the use of metal cavities, which has led to impressive OPD photoresponse. These have pushed OPD response far beyond the band-gaps of the composing materials with significant EQE responses of around 20-40%^{.31,94-96}. Not only do they achieve high EQE values significantly below the band gap of the composing materials, but by accurately controlling the cavity dimensions, basically by modifying the thickness of the electrodes and the active layer, the detection wavelength can be finely ~~tuned~~ ^{Ref's here?} ~~tuned~~. Despite the remarkable performance of optical microcavity based devices, the nature of an optical cavity makes the resonant frequency critically dependant on film thickness. For that reason, these devices will, most likely, not be compatible with techniques such as roll-to-roll processing, in which thicknesses usually fluctuate within a certain tolerance, and making that tolerance tighter comes at great cost.

at great costs
or
at a great cost

In this thesis, inspired by the micro-cavity devices and the work performed in the previous section, we have explored a device configuration that enhances CTS absorption by nanostructuring the active layer and the back electrode in the shape of a photonic crystal.⁹⁷ Photonic crystals are not an entirely new concept within photovoltaics, as some major accomplishments have been achieved already by nanostructuring photovoltaic devices.⁹⁸⁻¹⁰¹ In this thesis, however, we developed a photodetector with a nanostructured active layer and back-electrode with a nanostructure consists of a 2D periodic photonic crystal. This photonic crystal has been engineered to couple incident light into photonic modes that provide electric field concentration in the photoactive medium, within the wavelength range of the CTS absorption of our materials. In order to fulfill real application requirements, our devices have been mainly fabricated with low cost active layer materials, using inexpensive and scalable techniques such as blade coating for the photodetector manufacturing and nanoimprinting soft lithography for active layer nanostructuring.^{56,58,102,103}

Our devices are based on a bulk hetero-junction (BHJ) architecture, consisting of an electron

donor PBTTT or P3HT and an electron acceptor PC71BM or PC61BM. We have been able to easily and seamlessly nanostructure these active layers via soft nanoimprinting lithography, leading to a significant increase in EQE response within the NIR, from 750 to 1000 nm and from 775 to 1075 nm, for P3HT:PC61BM and PBTTT:PC71BM, respectively. This photore-sponse increase can be attributed to the absorption of the CTS, since it is significantly beyond the band gap of the individual active layer materials. We have also used different nanostructure lattice parameters to select the wavelengths where the absorption would be enhanced, providing us with wavelength response tunability on the NIR region.

Finally, we demonstrated that, in our devices, enhanced photodetection wavelengths are thickness variation tolerant within a certain range. This means that processing tolerances can be higher, making this device attractive for further development and commercialization. In summary, the designed and implemented light trapping configuration enables us to use inexpensive organic materials for light detection within the NIR wavelength range with minimal disruption of the fabrication process, where the nanostructuring step does not negatively affect the electrical performance of the photodetector.

1.4.2 Device Fabrication

Materials

The OPD active layer was composed of either P3HT:PC61BM or PBTTT:PC71BM BHJ blends. These materials were chosen because of several reasons: first, they are really affordable and widely available materials, which makes them appealing for further development and upscaling;⁶⁰ second, these specific combinations show a significant CTS absorption tail that extends into the NIR region, which means that we can enhance this absorption, and extend the response of the devices beyond their individual band gaps;³¹ and third, their high carrier mobilities allow

us to deposit thick active layers, which is an essential aspect to make the most out of the CTS low absorption coefficient.⁸⁴

Other material blends such as P3HT:OIDTBR were also explored, however due to their respective HOMO/LUMO level arrangement being more closely matched, their charge transfer state did not extend deep into the NIR.¹⁰⁴ That is why, after the first failed trials, they were quickly discarded in favour of fullerene-containing active layer blends.

While the general manufacturing procedure, which has been explained in detail in section 1.2: Materials and Methods, is common amongst devices manufactured within this chapter, our nanostructured photodetector fabrication process has some specific characteristics.

The first is their thick active layer ($\sim 1\mu m$), which in general is one order of magnitude thicker than the solar cells manufactured in the previous section, and that of most reported organic solar cells.^{105,106} Besides, the active layer nanostructuring of our photodetectors is performed via soft nanoimprinting lithography, when the active layer is completely dry and all the solvent is fully evaporated, like we did with the PBDBT:ITIC blends. With this reliable and roll-to-roll compatible technique,^{102,107} we did not require a cleanroom to fabricate our devices, yet we could produce extensive nanostructured areas with high fidelity and reproducibility.

After device encapsulation, we performed a thermal annealing to increase the active layer crystallinity and enhance charge transport properties. The back electrode, being deposited onto the nanostructured active layer, adopted the shape of the nanostructure (figure 1.8) which provided the sample with a strong optical response.

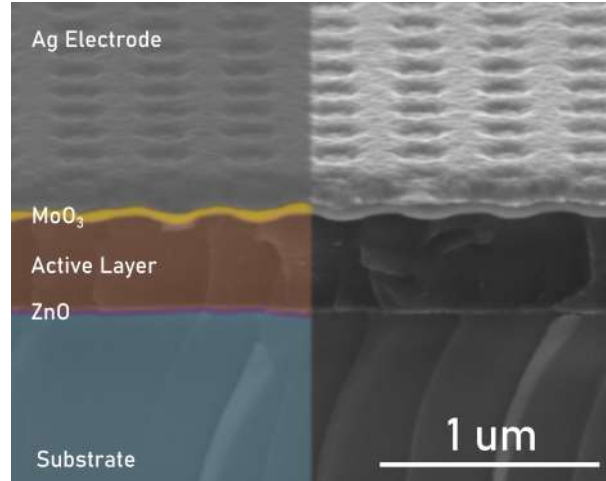


Figure 1.8: Cross-section SEM image of a nanostructured photodetector with all the conforming layers colorized for better visualization. The lowermost ITO layer is missing because the image was taken in a ITO free area of the patterned substrate.

SEM Images

Topology pictures obtained with the SEM, confirmed that the nanoimprinting lithography was reliable and reproducible. We can see in the SEM images that the nanostructure is practically perfectly reproduced on both the active layer and the back electrode (figure 1.8). These structures exhibit a continuous square lattice pattern over an extensive area with minimal defects. This is mainly thanks to the reliability of the soft NIL technique that we use on the fabrication of such devices, and further proves its reproducibility and viability as a large scale manufacturing technique.

SEM cross-section images provide us with a lot of information about both layer composition and thickness. As we see in figure 1.8, layers are not only clearly defined, but the nanostructure is really visible and easily identifiable on both the active layer, and the back electrode, with the thin HTL being sandwiched in the middle. These cross-section images were crucial determining the complete coverage of the active layer by the HTL as we discussed in section ??: ??.

Nanostructure Design

In order to have a significant response on the NIR region, we need to nanostructure the active layer of the device to provide it with light trapping properties at wavelengths below the band gap of the BHJ materials. We decided to use a nanostructure composed by an array of cylindrical pillars that collectively act as a diffraction grating, in-coupling light into propagating modes within the active layer. With Finite-Differences Time-Domain method (FDTD), performed by Dr. Molet, we were able to engineer the optimal photonic structures for our photoactive materials while we got useful insights about light propagation within the device. As a result of our simulations, we decided that array lattice parameters (L) of 400, 500 and 600 nm (from now on also referred to as L400, L500 and L600) provided guided modes with a wide enough wavelength range within the NIR region. We can see in figure 1.9 that their first order of diffraction is distributed along the absorption range of the CTS of our active materials. This in coupling phenomenon provides efficient light trapping at specific wavelength ranges below the band gap of the active layer materials, thus selectively enhancing CTS absorption.

The photonic crystal is able to change the momentum of impinging light by 1.57 cm^{-1} for $L = 400 \text{ nm}$, 1.25 cm^{-1} for $L = 500 \text{ nm}$ and 1.05 cm^{-1} for $L = 600 \text{ nm}$ for the first diffraction orders. This extra parallel momentum added to the initial $\vec{k} = 0 \text{ cm}^{-1}$ (in the studied case of normal incidence) gives the ability for specific wavelengths to be incoupled to guided modes within the active layer. These specific wavelengths are 750 nm, 835 nm, and 1010 nm for L400, L500 and L600 respectively, for the case of P3HT:PC61BM (figure 1.9 a)) and 775 nm, 900 nm and 1080 nm for L400, L500 and L600 respectively, for PBTTT:PC71BM (figure 1.9 b)). These wavelength values are in good agreement with the EQE NIR peaks shown in following section's figure 1.12 (EQE Curves), for each lattice parameter and active layer material.

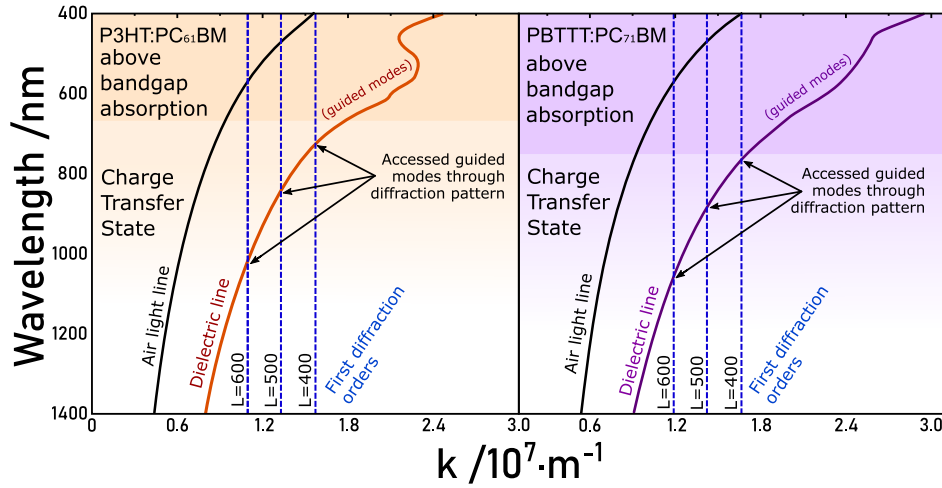


Figure 1.9: Dispersion relation of the wavelength vs parallel wavevector of the incident light for a) P3HT:PC₆₁BM and b) PBTTT:PC₇₁BM blends. The first diffraction orders of the photonic crystal arrays with lattice parameters of 400, 500 and 600 nm (blue dashed lines) grants to the incident light the necessary momentum to couple to the guided modes within the semiconductor material in the CTS range of absorption (a) red and b) purple lines). Figure adapted from: J. Mater. Chem. C, 2020, 8, 9688¹

Simulations

In order to calculate the potential enhancement of the CTS absorption we decided to perform some optical simulations for our photodetector device. These simulations were performed using Finite-Differences Time-Domain method (FDTD) in collaboration with my fellow colleague, Dr. Molet.

The simulations consist of two full device layer stacks, one with a shallow 60 nm nanostructure and the other without any nanostructure at all. The lattice parameter we chose for the simulations was L500, because it was located in the middle of our range and the expected absorption enhancement fell not too far nor too close from the absorption tail of our materials.

We can see in the simulations that the calculated absorption spectrum of the L = 500 nm PBTTT:PC₇₁BM shows a series of peaks around 900 nm that correspond to the resonance modes seen in figure 1.10. These peaks are in good agreement with the measured external

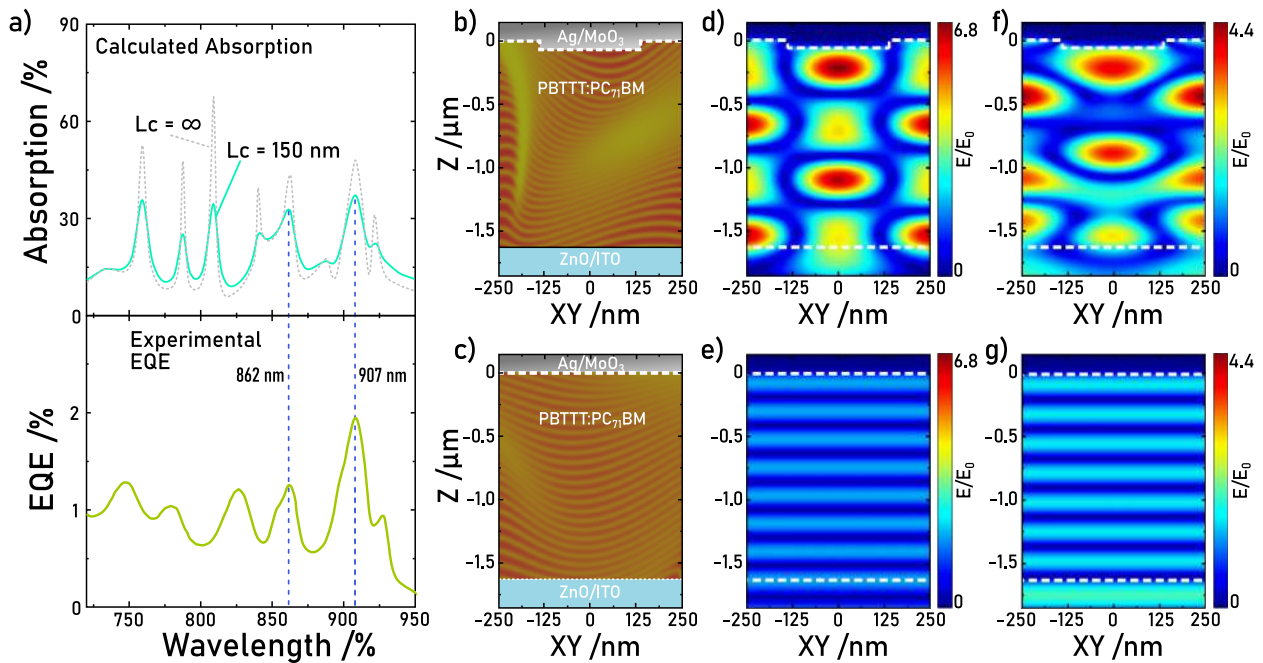


Figure 1.10: (a) Calculated absorption of the fabricated devices with fully coherent light (grey dashed) and 150 micron coherent light (red). (b) External quantum efficiency measurements for a PBTTT:PC₇₁BM nanostructured photodetector with a lattice parameter of $L = 500$ nm. Sample scheme for nanostructured and flat devices (c), (d) and calculated electric fields at wavelengths 862 and 907 nm (e), (f) and (g), (h). Figure adapted from: J. Mater. Chem. C, 2020, 8, 9688¹

quantum efficiency that we will see in later subsections, confirming the effect of the photonic architecture within our device. We also examined the spatial distribution of the electric fields at the wavelengths of maximum response, which correspond to resonant modes. The electric field distribution at 862 nm and 907 nm is represented for both the nanostructured and the flat devices. In the planar device, the electric field presents a standard plane wave distribution, while in the nanostructured devices a diffraction pattern appears inside the active layer, with field enhancements of around 6 times the incident power. This leads to the conclusion that the enhanced optical path in the active layer, caused by the diffraction modes of the nanostructure, will provide a higher CTS absorption within the studied wavelength ranges.

1.5 Nanostructure Electrical Optimization

While it was outside the scope of this thesis to perform a full photodetector optimization, in order to manufacture functional devices, certain parameters required optimization. The main three parameters to be optimized were the active layer of our devices, their dark current and annealing conditions, namely temperature and time. While this process is briefly summarized in this section, a further detailed explanation can be found in the appendix of this chapter.

The first parameter that needed optimization was the dark current, which was significantly higher in nanostructured devices than in their flat counterparts. Since the dark current of a device ultimately limits its lowest detection threshold, also known as its noise equivalent power, we are interested in decreasing it as much as possible.¹⁰⁸ However, the higher dark currents present in our nanostructured photodetectors increased their noise, raising its detection threshold. We attribute these high dark currents to the high current leakage caused by a non conformal coating of the HTL. In this way the back electrode was in direct contact with the active layer, hindering the function of the HTL.

After exploring various approaches such as depositing thicker hole transport layers, or manufacturing our photodetectors with a Schottky barrier, the most effective solution was to make the nanostructure features shallower. These shallow nanostructures were conformally coated by the HTL with a similar optical response, which resulted in much lower dark currents of around 10 nA cm^{-2} with a reverse bias of 1 V and $1 \mu\text{A cm}^{-2}$ at 15 V, with similar electrical performance to the non nanostructured photodetectors.

The active layer thickness was another characteristic that required optimization, because of the compromise between the low absorption coefficients in the NIR and the low charge mobilities in organic semiconductors.⁵ On one hand, the NIR absorption coefficient of our active layer materials is really low, so active layers need to be thick to efficiently absorb in this wavelength range. However, since the charge mobility of organic semiconductors is also limited, a really thick active layer will exhibit lower charge extraction efficiencies, limiting device performance.

In order to balance these two factors, we manufactured several nanostructured devices with different active layer thicknesses and measured their EQE enhancement factor. This factor is the relation between the EQE of the nanostructured photodetectors and EQE of the flat photodetectors in a given wavelength. These devices showed reduced dark currents and great EQE enhancement factors in the NIR, with an optimal active layer thickness of 700 nm for P3HT:PC61BM and 1600 nm for PBTTT:PC71BM, which were used in the rest of the study. These difference in optimal active layer thickness is attributed to the higher charge mobility of PBTTT:PC71BM when compared with P3HT:PC61BM.

As a side result of this optimization, we confirmed that the active layer thickness does not significantly affect the central peak wavelength where the EQE is enhanced, as opposed to other devices previously reported in the literature, making this process interesting for manufacturing purposes.

Finally, we optimized the annealing characteristics for the active layers. This procedure is used to control the active layer crystallinity, which greatly affects the performance of OPV devices, making it a common procedure in the world of OPV.¹⁰⁹ In this study we have seen that both P3HT:PC61BM and PBTTT:PC71BM active layers exhibit enhanced performances after the annealing process. These show increases of up to 1.8 fold and 8.7 fold for P3HT:PC61BM and PBTTT:PC71BM respectively. This process proved to be a crucial step, especially for PBTTT:PC71BM where the intermixing greatly affects the CTS absorption.

In summary, devices were manufactured as explained in section 1.4.2: Materials, with an active layer thickness of 700 nm for P3HT:PC61BM and 1600 nm for PBTTT:PC71BM. We used the same annealing process for the two materials at a temperature of 135°C for 20 minutes.

1.5.1 Device Characterization

FTIR Spectra

In order to evaluate the optical performance of our devices, as well as the reliability of our nanoimprinting method, we used both the SEM, as we have seen in previous sections, as well as FTIR spectroscopy, to measure transmission and reflection spectra.

The various FTIR spectra obtained from flat and nanostructured OPDs immediately indicate that the optical properties are significantly dependent on the lattice parameter. This difference is apparent already with the naked eye (figure 1.11 (right)). As we can see in figure 1.11 (left), the difference between flat and nanostructured devices is clearly noticeable, especially on the NIR region where our photonic crystals have been designed to have maximum light absorption.

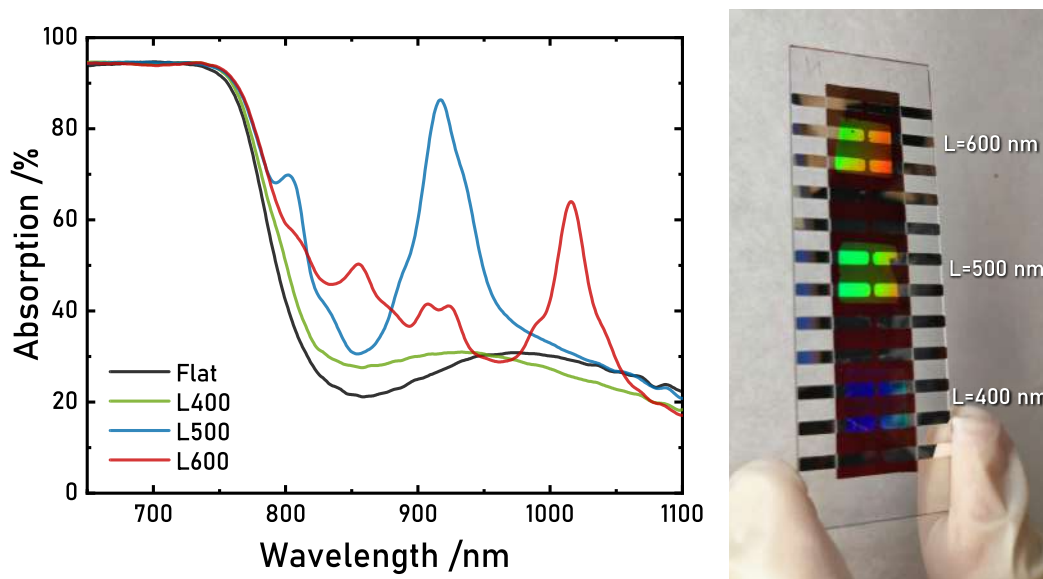


Figure 1.11: FTIR absorption spectra of PBTBT:PC71BM based devices for various nanostructure lattice parameters as well as flat reference (left). Picture of a finished device exhibiting different iridescence characteristics for different photonic crystal lattice parameters. From top to bottom: $L = 400$, $L = 500$ and $L = 600$ nm (right).

Not only do we have significant absorption peaks, but their wavelength behaviour is also in agreement with our initial hypothesis, where the absorption peak of largest lattice parameter nanostructure ($L600$) is further into the infrared, whereas $L500$ is much closer to the visible. While these peaks are clearly visible, the peak for $L400$ has been completely overshadowed by singlet absorption. Finally, we can observe the weaker higher order absorption peaks, for both $L500$ and $L600$, which are closer to the visible but are much weaker than the main peak.

EQE Curves

One of the most important features of photodetectors in general is their spectral response. That is why EQE curves are one of the most useful pieces of information for any photodetector.^{110–112} The EQE curves extracted from our nanostructured OPD devices showed several peaks in the NIR that were absent in the reference flat samples (figure 1.12). These peaks were present for both active layer compositions, and they were consistently present on nanostructured devices with different lattice parameters, while being completely absent in any of the flat samples. That led us to the conclusion that they must have been related to the nanostructured active layer

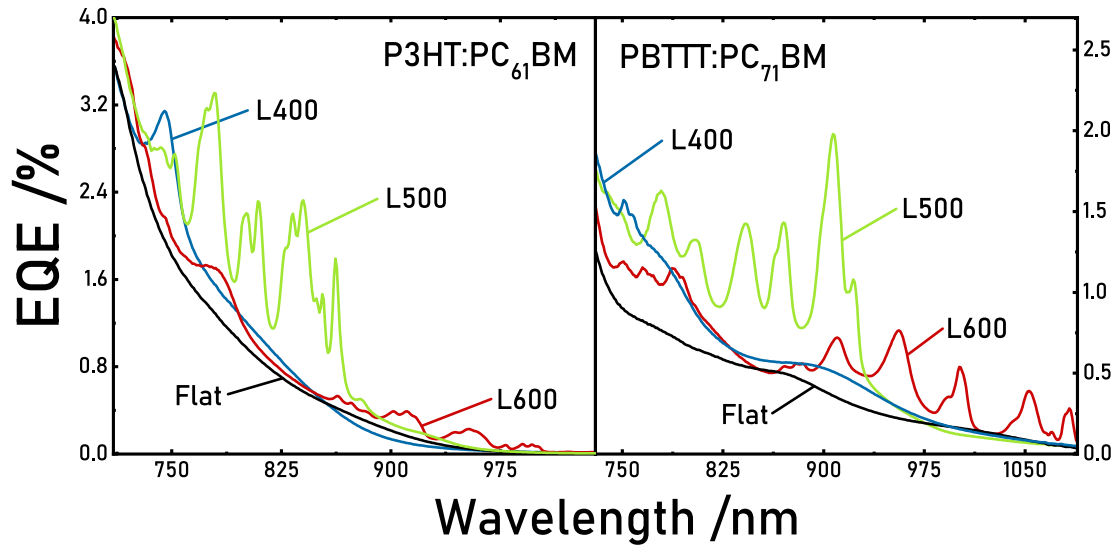


Figure 1.12: External quantum efficiency measurements for non-structured (flat) and differently nanostructured photodetectors (L400, L500 and L600) with an active layer of P3HT:PC₆₁BM (left), PBTTT:PC₇₁BM (right). Figure adapted from: J. Mater. Chem. C, 2020, 8, 9688¹

and back electrode configuration.

In the same graph, we see that the spectral range, at which the EQE is enhanced by the photonic crystal structure, is clearly dependant on the lattice parameter of the nanostructures, as well as the refractive index of the active layer, as predicted by our previous simulations. We see that EQE enhancement peaks are red-shifted with larger lattice parameters and higher active layer refractive indexes, in accordance with our initial hypothesis.

Devices with the shortest lattice parameter (L400) are the ones that exhibit the lowest enhancement factor of around 1.6 and 1.7 fold for P3HT:PC₆₁BM and for PBTTT:PC₇₁BM respectively (figure 1.13). This enhancement is located within the tail of the singlet absorption, hence it is overshadowed by its performance. Nevertheless, in that same figure we can clearly distinguish a narrow peak located at 750 nm for P3HT:PC₆₁BM and two twin peaks between 750 nm and 775 nm for PBTTT:PC₇₁BM that indicate a small enhancement.

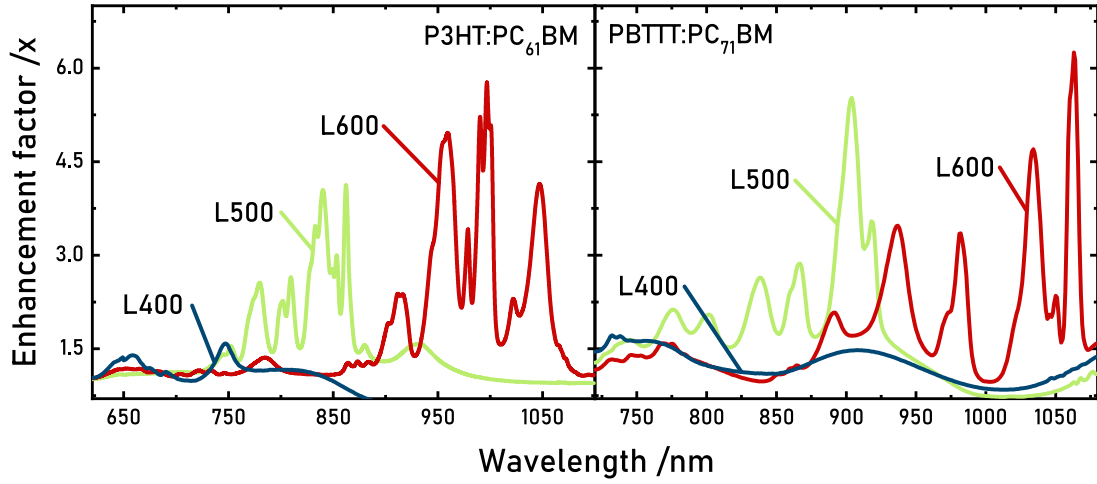


Figure 1.13: Ratio between nanostructured and flat EQE curves (Enhancement Factor) for three different lattice parameters and two different active layer materials; P3HT:PC₆₁BM (left), PBTTT:PC₇₁BM (right).

For devices nanoimprinted with the $L = 500$ nm photonic crystal, the enhancement is much more pronounced. We can see in figure 1.12, that their EQE peaks reach over 2% for both PBTTT:PC₇₁BM and P3HT:PC₆₁BM, while being well below their respective band-gaps. Their flat counterparts on the contrary, show much lower EQE values around 0.4% on the same wavelength region. The enhanced photoresponse of P3HT:PC₆₁BM based devices in the 800–850 nm region (figure 1.12 (left)), shows a 4-fold enhancement factor at its maximum at 837 nm (figure 1.13 (left)) when compared to the flat reference sample, achieving a maximum absolute EQE value of 2.4%. For the same lattice parameter, devices based on PBTTT:PC₇₁BM exhibit EQE peaks deeper into the NIR (850–920 nm), with a 5 fold increase on efficiency at its maximum at 907 nm, reaching absolute EQE values of slightly over 2% (figure 1.12 (right) and figure 1.13(right)).

Finally, nanoimprinted devices with $L = 600$ nm lattice parameter show EQE enhancement peaks that reach a lot deeper into the NIR, around 900–1050 nm for P3HT:PC₆₁BM and around 950–1100 nm for PBTTT:PC₇₁BM. However, since absorption in this region is very limited, EQE values only reach maximum values of around 0.5% (figure 1.12 red lines). This lower overall performance can be attributed to the lower values of the CTS absorption coef-

ficient at higher wavelengths, being lower for P3HT:PC61BM than for PBTTT:PC71BM.³¹ Even though the absolute performance in these regions is lower than that of smaller lattice parameters, it is worth noting that the enhancement effect is the greatest. We see that in P3HT:PC61BM based devices, EQE peaks have a local maximum at 1000 nm where a 5.8 fold enhancement is reached (figure 1.13 (left)). And for PBTTT:PC71BM based devices, performance is 6 times better than its flat counterpart (figure 1.13 (right)).

We decided to focus our efforts on continuing with a full electrical characterization of the PBTTT:PC71BM L500 photodetector, since it was the one that exhibited the most interesting characteristics, having peaks far on the NIR region while still maintaining a significant EQE response.

Photoconductivity

In order to increase the response of our photodetectors, it is an interesting strategy to measure their EQE in a photoconductive mode, with a reverse V bias. In this mode we can enhance charge extraction in our devices, overcoming their low overall mobilities, particularly undesirable in thick active layers, while keeping the reverse V bias within **real** operation values. We can see that, the EQE of our nanostructured photodetectors increases from $\sim 2\%$ to 7.5% at its peak in 907 nm, while the flat reference still lays below the 2% mark upon applying a 23 V reverse bias (figure 1.14). The fact that the spectral response is completely independent from the applied bias, confirms that the enhancement is based on a purely optical phenomenon.

Responsivity

As we have discussed in section ??, another interesting figure of merit which provides insight about photodetectors is the spectral responsivity. For our photodetectors, we measured the

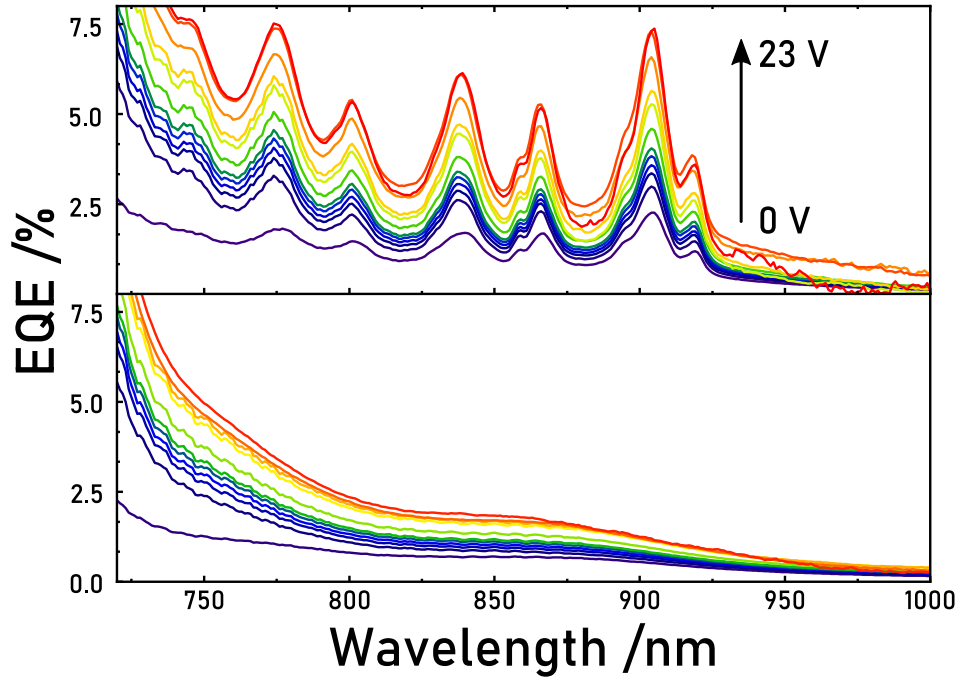


Figure 1.14: EQE measurements with various reverse applied V bias from 0 V to 23 V for (top) nanostructured and (bottom) non-structured (flat) PBTBT:PC71BM photodetectors. Figure adapted from: J. Mater. Chem. C, 2020, 8, 9688¹

responsivity at different reverse bias voltages in order to measure its saturation value for both flat and nanostructured devices.

We have observed that, in our organic photodetectors, responsivity saturation occurs at much higher bias voltages for nanostructured devices (28 V) than those of planar devices (12 V) (figure 1.15 (right)). This further confirms that charge generation enhancement comes from the nanostructure since, as stated in section ??: ??, at high reverse V bias the vast majority of charges generated by the photodetector are efficiently extracted. That is why, we can attribute the higher responsivity saturation to an enhanced absorption within the active layer, since a higher amount of generated charges requires a higher reverse bias to fully extract them all.

If we compare the responsivity of flat and nanostructured devices, we can also see that the nanostructured, $L = 500$ nm PBTBT:PC71BM based device, shows a responsivity of 15 mA W^{-1}

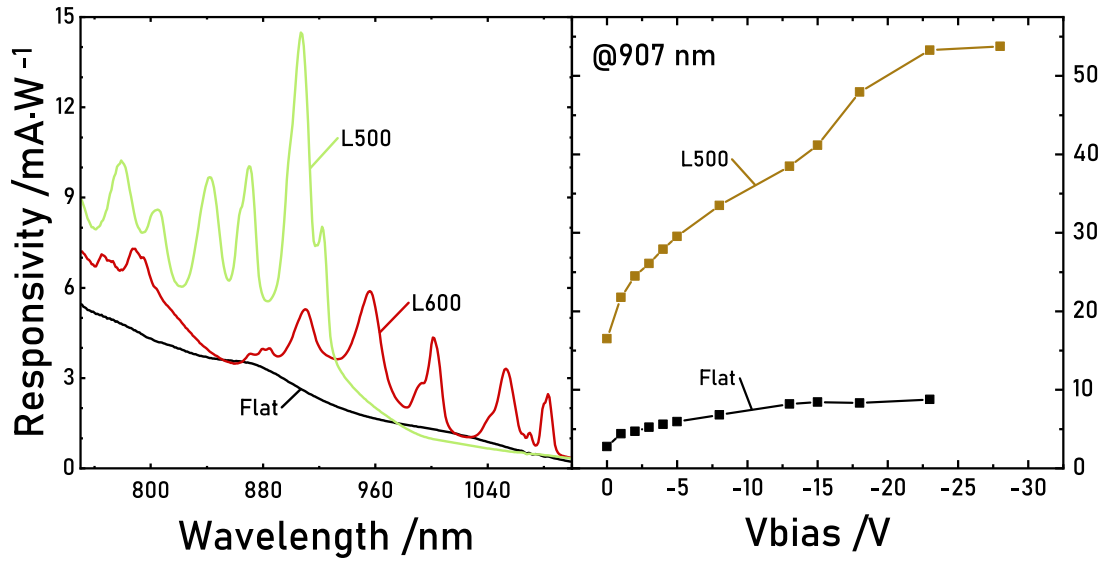


Figure 1.15: Responsivity of PBTTT:PC71BM photodetectors at different wavelengths for both nanostructured and flat devices at zero V bias (left). Responsivity at 907 nm for different V bias of L = 500 (nanostructured) and non-structured (flat) PBTTT:PC71BM photodetector (right). Figure adapted from: J. Mater. Chem. C, 2020, 8, 9688¹

while its flat counterpart exhibits only 3 mA W⁻¹ at 907 nm. (figure 1.15 (left)). We can increase the responsivity with a reverse bias, which, at its saturation point of 23 V, reaches 54 mA W⁻¹ for the nanostructured device, versus the 9 mA W⁻¹ that the flat counterpart exhibits at the same voltage (figure 1.15 (right)).

Even though the performance of our OPDs is still low compared to that of singlet absorption based OPDs, our device performance is on the same order of magnitude as that of OPDs reported in the literature that use similar strategies, such as those reported by Meridith et al.² Furthermore, our nanostructured OPD performance on the NIR is similar to other CTS absorption based photodetectors that need to work under extremely high reverse biases of up to 200 V.^{93,113}

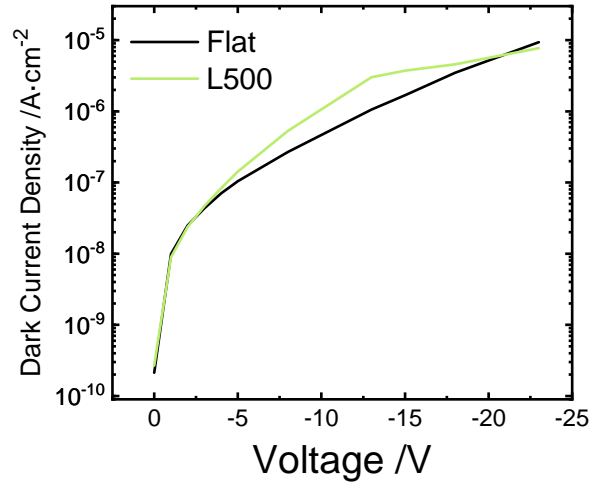


Figure 1.16: Dark current of both flat and $L = 500$ nanostructured devices at various reverse V bias. Figure adapted from: J. Mater. Chem. C, 2020, 8, 9688¹

Dark Current

The main problem with the nanostructuration process has been the formation of pinholes within the HTL due to inhomogeneous coverage, as discussed in section 1.5: Nanostructure Electrical Optimization.

However, after solving the major issues related to pinhole formation, we are left with similar dark currents for both nanostructured and flat devices (figure 1.16). Considering the large area of our photodetectors (8mm^2), the measured dark current is rather low at 10 nA cm^{-2} with a reverse bias of 1 V and $1\text{ }\mu\text{A cm}^{-2}$ at 15 V . These values are on the same order of magnitude as those reported in the literature for these materials.^{114–118} Especially considering the fact that, with solution processing, dark current does not tend to scale monotonically with photodetection area. Mainly because there is a much higher probability of defect formation on larger devices, which leads to a dramatic increase in dark current.¹¹⁹

On/Off Ratio

The On/Off ratio is the ratio between the signal and the noise power levels at given light power density conditions. It gives an intuitive feeling of how much effective signal does our photode-

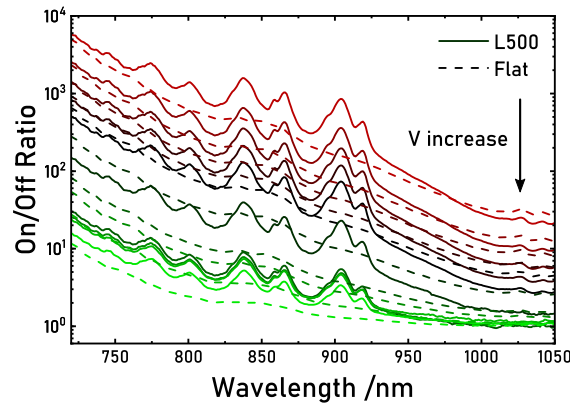


Figure 1.17: On/Off ratio of flat (dashed line) and L500 PBTTT:PC71BM based nanostructured devices at different wavelengths for various reverse V bias voltages from 1 V (red) to 23 V (green). Figure adapted from: J. Mater. Chem. C, 2020, 8, 9688¹

tector produce when exposed to a certain amount of light. The illumination conditions are set to the wavelength of maximum EQE enhancement and the setup's maximum available power.

By significantly lowering the dark current of our devices with our brief optimization, we have been able to increase the on/off ratio of our nanostructured photodetectors to up to 850 for our L500 devices at -1 V and 907 nm, when illuminated with 3.5 mW cm^{-2} . That value is 5.5 times higher than the one measured in our flat photodetectors ($\text{On/Off ratio}_{\text{flat}} = 150$) which further confirms that the dark currents after the nanostructuring process are similar as before, while the responsivities are enhanced. These values are on the same order of magnitude as other organic photodiodes reported in the literature such as those reported by Zhu et al. and Jahnelt et al.^{120,121} In the case of L600 based devices, the on/off ratio is drastically reduced due to the reduced absorption on the deeper NIR region, however it is still at 15 for the nanostructured photodetectors, while in our flat equivalents the on/off ratio is just 3. The on/off ratio is still consistently superior in the case of our nanostructured OPDs at higher reverse biases, as we can see in figure 1.17. However, as it is usual with these kind of photodiodes, the noise escalates faster than the signal under high reverse biases, so the overall on/off ratio decreases with the applied voltage.

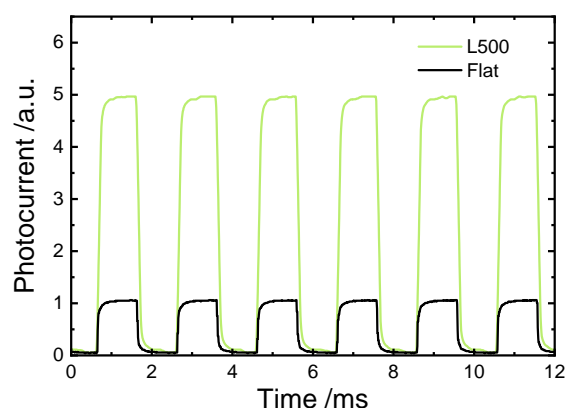


Figure 1.18: Time dependent normalized photoresponse measurement for both flat and $L = 500$ PBTTT:PC71BM based nanostructured devices at 0 V bias. Figure adapted from: J. Mater. Chem. C, 2020, 8, 9688¹

Transient Response

Apart from all the static electrical characterization, we evaluated the time response of our photodetector. While performing a full frequency study is outside the scope of this work, we wanted to have a rough estimate of the frequency range in which our photodetector could operate. The main motivation of this test is that the low mobilities and large area of our photodetectors could lead to a slow response, and nanostructuring the back electrode, hence increasing its surface area had the potential to considerably increase the OPD's capacitance, ultimately hindering device response time.¹²²

Thankfully, upon measuring transient photocurrent, our OPDs exhibit response times on the order of a hundred microseconds at 0 V bias, which were approximately equal in both nanostructured and flat devices (figure 1.18). These results confirm that the capacitance of our devices is not significantly affected by the nanostructuring of the active layer. We chose to perform these measurements at a 0 V bias because photodiodes tend to exhibit their slowest responses when no external field is applied.

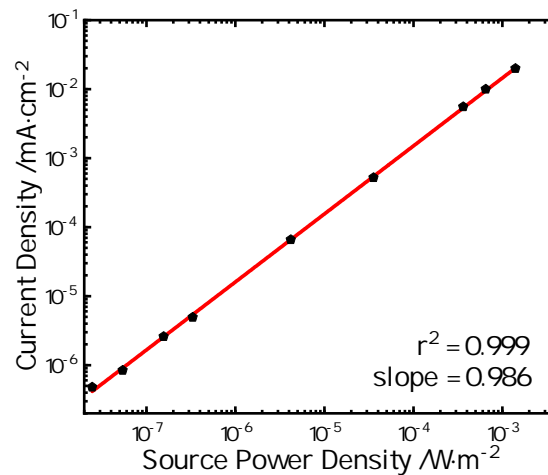


Figure 1.19: Measured linear dynamic range of L500 PBTTT:PC71BM nanostructured photodetector at 0 V bias. Figure adapted from: J. Mater. Chem. C, 2020, 8, 9688¹

Light Dynamic Range

For the sake of completeness we measured the linear dynamic range of our nanostructured photodetectors.

As we can see in figure 1.19, the response of our nanostructured OPDs is linear within our measuring range of 50 dB, exhibiting an r^2 value of 0.999 and a slope of 0.986, for the case of an L500 nanostructured device, illuminated with monochromatic light at 907 nm. The combination of the r^2 value and the fact that the slope is really close to 1, confirms that the response of our photodetector is highly linear within the measuring range.

We must say that our setup was somewhat limited in the power output range available, so this linearity will most likely extend further in both directions when measured with the proper setup.

1.5.2 NIR Multiwavelength Photodetector

As a final test, we decided to evaluate the spatial homogeneity of our nanostructuring technique, and the resulting photodetectors. For that we fabricated large continuous photodetectors on a microscope slide (as described in section x) and we nanostructured areas of 1 cm^2 with the three different lattice parameters, L400 L500 and L600, while leaving the rest of the photodetector area flat, to be used as a reference. We chose to use PBTTT:PC71BM as our active layer material, since it exhibited the best CTS enhancement at higher wavelengths.

In order to measure the spatial distribution of the photodetector's performance, we used the technique discussed in chapter ??: ?. We must say, however, that, due to the highly localized nature of these measurements, they had to be performed with a low magnification microscope objective which slightly changed the wavelength dependence of our photodetectors' EQE enhancement.

We can clearly see in figure 1.20 that the nanostructured regions of the photodetector exhibit an enhanced EQE response on the NIR region when compared to the flat areas surrounding them. On top of that, we can also see that the overall enhancement and performance are rather homogeneous along the photodetector, with small gradual shifts that we can attribute to slight thickness variations, resulting from imperfections during the blade coating process. The latter further confirms that EQE enhancement is not strongly related to thickness variations, but is completely derived from the nanostructuration of the active layer.

A deeper analysis of the photodetector response at different excitation wavelengths, clearly reveals how the absorption enhancement of the CTS greatly depends on the lattice parameter, as we have seen with previous EQE data (figure 1.12). If we carefully examine each LBIC map with different excitation wavelengths, we can see that, when illuminating with light at 710 nm,

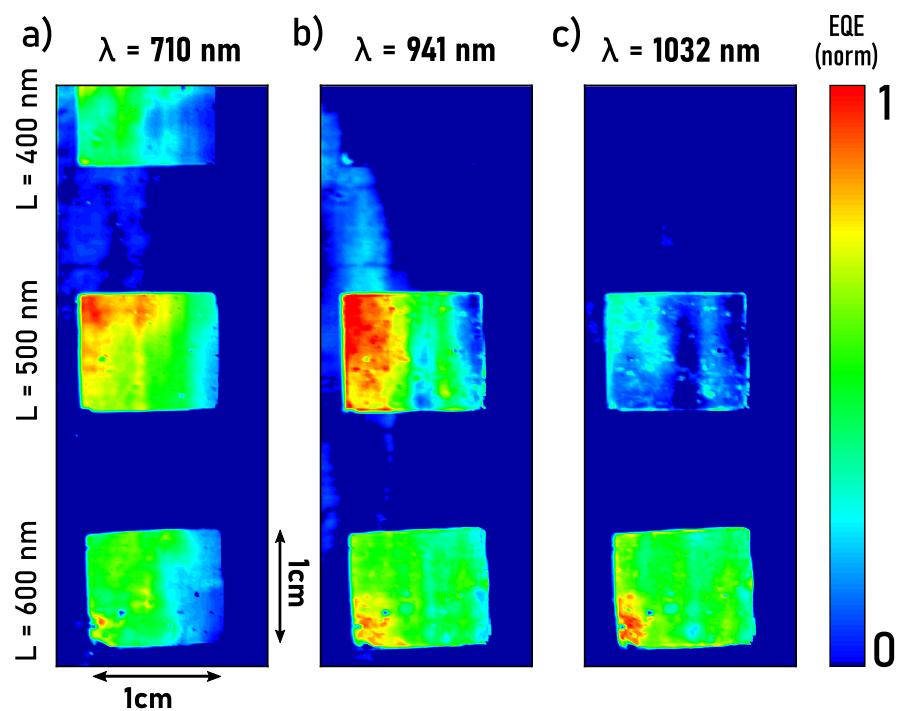


Figure 1.20: Light beam induced photocurrent (LBIC) maps of a large area continuous back electrode photodetector, at 3 different excitation wavelengths: (a) 710 nm, (b) 941 nm and (c) 1032 nm, with 3 different nanostructured zones. From top to bottom: $L = 400$, $L = 500$ and $L = 600$ nm. Figure adapted from: J. Mater. Chem. C, 2020, 8, 9688¹

all three patterns exhibit similar responses, since they all provide diffraction at these wavelengths where singlet tail absorption is still present (figure 1.20 (a)). Even though there is not a clear difference between the patterns, they all significantly outperform the non patterned regions, which are depicted in blue around the nanostructured regions due to their lower photoresponse. We attribute this generalized enhancement to the fact that, even though the magnification of the microscope objective is low, the slight angle range at which light impinges on the substrate increases the probability that, at least some photons have the right \vec{k} vector for being in-coupled into the active layer.

When we increase the wavelength, however, we start to clearly differentiate the diffraction capabilities of the different lattice parameters, since, with an illumination wavelength of 941 nm, the diffraction modes of the L400 nm are not able to incouple such large wavelength photons. That is why we cannot see any response enhancement in that region of the map, while L500 and L600 are still able to incouple most of the NIR light, still with a remarkable enhancement (figure 1.20 (b)). Nevertheless, we clearly see that, even though both lattice parameters exhibit an enhanced response, L500 shows the highest photocurrent at this illumination wavelength. Further confirming the results obtained previously in 1.5.1: EQE Curves.

Finally, when we increase the wavelength all the way up to 1031 nm, the only region that still exhibits a significantly enhanced response is the region nanostructured with the L600 pattern. The other two regions are practically invisible in the image, fact that is in accordance with all previous electrical characterization results (figure 1.20 (c)).

Interestingly, each lattice parameter presents an enhanced response in different parts of the spectrum, in a series of peaks within a narrow range. That means that, in this device, each 1 cm^2 'pixel' responds to different parts of the spectrum, so, if calibrated using the EQE data, one could devise a way to manufacture a monolithic spectrometer based on only one active

layer material, but three (or more) pixels that could emulate the RGB strategy, but on the NIR. Thus the photodetector of figure 1.20 can be considered as a crude artificial NIR eye.

1.6 Conclusions

In this chapter, we have explored the possibility of nanostructuring the active layer of organic solar cells based on different active layer blends. The nanostructuring of P3HT:PC61BM solar cells resulted in an enhanced J_{sc} which is in accordance with previous simulations. However, nanostructured solar cells exhibited a lower FF, attributed to higher leakage currents than their flat counterparts. The resulting nanostructured solar cell efficiencies were similar for both nanostructured and flat devices, suggesting that, with further optimization, a higher efficiency nanostructured device is feasible.

Even though it has not resulted in a significant increase in efficiency for P3HT:PC61BM based organic solar cells, there has not been a significant decrease in efficiency, which proves that the nanostructuring process is feasible and its effects on the electrical properties of the cell are minor.

On the other hand, we have reported a new organic photodetector architecture, based on an inverted BHJ, which is capable of detecting light at wavelengths significantly below the band gap of either of its active layer components. This has been achieved by enhancing the absorption, and subsequent electrical response, of the CTS absorption present in active layer blends based on P3HT:PC61BM and PBTTT:PC71BM. This CTS absorption enhancement was achieved by the incorporation of a photonic nanostructure within the active layer of the device via soft nanoimprinting lithography. Active layer deposition, and subsequent nanostructuration, were performed using highly scalable, roll-to-roll compatible techniques, which increase the industrial appeal of our devices.

We also performed a limited optimization study, that resulted in fully functional nanostructured devices with dark currents similar to their flat equivalents. Besides, nanostructuration driven EQE enhancement wavelength range proved to be rather insensitive to thickness variations, offering appealing fabrication tolerances, further increasing its commercial potential. Furthermore, we have used active layer materials that are inexpensive, simple and easy to produce, which makes them ideal for large scale manufacturing.

Several critical measurements such as photodetector detectivity or the complete dynamic range measurement could not be performed because they required the use of specialized equipment and expertise which we did not possess at the time of the experiments. Despite these limitations, we do believe that our characterization provides meaningful insight and thoroughly describes the behaviour of our photodetectors. The variety of techniques used to characterize our photodetectors concur on the superior performance of nanostructured OPDs on the NIR spectral region when compared with their flat counterparts, mainly due to an enhanced CTS absorption.

On top of that, we have been able to enhance the CTS absorption of our devices at different wavelength ranges, in a controlled manner, by changing the lattice parameter of our nanostructure. This capability allows us to accurately tune the wavelength response of our NIR photodetectors by enhancing the electrical response in the wavelength range of interest. In summary, we have developed wavelength tunable NIR organic photodetectors by making use of CTS absorption and photonic crystals, opening new opportunities for the use of active layer materials beyond their individual band-gaps.



Appendix

This appendix summarizes some of the efforts and the experiments performed in order to optimize the incorporation of nanostructures into the active layer of organic photodetectors. In particular, it explores the role of the HTL layer thickness and composition, the photoactive layer thickness, and the nanostructuring depth in the overall performance and EQE enhancement of the final devices.

1.A Nanostructure Electrical Optimization

The first problem we encountered with nanostructured photodetectors was that they exhibited really high dark currents, when compared to their flat counterparts. These were orders of magnitude higher than their flat, non-nanostructured, equivalent photodetectors. This would be a serious problem because photodetector performance is highly dependant on their dark current. Higher dark currents lead to higher noise levels which lead to lower signal to noise ratio and an overall reduced photodetector sensitivity.

We believe that this dark current increase on the nanostructured devices was mainly due to the introduction of pinholes in the hole transport layer. These pinholes would arise from the non-isotropic nature of the thermal evaporation process. As we have seen in chapter ??, thermal evaporation is a highly anisotropic process, where there is a clear preferential deposition direction. This means that the deposited thickness at any given point will depend on the angle

between the sample and the evaporation source. For a flat sample, if placed far enough from the evaporation source, the angle between the sample and the atoms coming from the evaporation source will be close to 90° , leading to a uniform thickness over the entire sample. However, if the sample is nanostructured with pillars, the pillar sides will be almost parallel to the path of the atoms coming from the evaporation source, greatly hindering the deposition capabilities on those areas.¹²³ Furthermore, if the pillars have a high aspect ratio, and are significantly taller than the deposited thickness, a non-conformal coating is almost guaranteed. When we combine this non-conformal coating, with the subsequent back electrode metal deposition, which is thick enough to completely cover the nanostructure, we end up with a situation where the back electrode is in direct contact with the active layer through the pillar sidewalls leading to extremely high dark currents (figure 1.22).

In order to reduce the dark currents caused by the nanostructuring process we followed several approaches. The first approach that we briefly explored was to use a fully metallic HTL trying to make a Schottky barrier. When a metal is placed in electrical contact with a semiconductor, the Fermi level of the semiconductor and the work function of the metal will align. If the metal work function is low enough, the semiconductor bands will bend upwards creating an electron barrier where the holes will be the major contributors to overall device current (figure 1.21 (right)). We decided to use gold, as it has one of the lowest work functions of all metals and it can be easily deposited by thermal evaporation. These Schottky barrier devices exhibited good overall performances in terms of external quantum efficiency, as well as a noticeable NIR EQE enhancement at zero v bias (figure ?? (left)). Nevertheless, as in most Schottky barrier based devices, the dark currents were still really high because of the lack of a semiconducting charge selective layer.¹¹⁹

The approach that gave the most desirable results, was to lower the nanostructure depth. By using RIE on our existing soft lithography stamps, as described in ?? : ?? we were able to manufacture a couple of nanostructured stamps with shallower features of 100 nm and 60 nm,

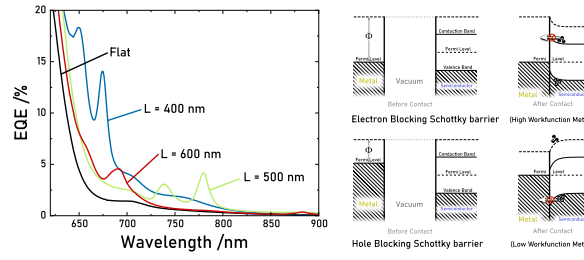


Figure 1.21: EQE enhancement peaks for a P3HT:PC61BM photodetector with a Schottky barrier formed between the active layer and the gold back electrode (right). Schottky barrier formation schematic diagram for metals with different workfunctions (left).

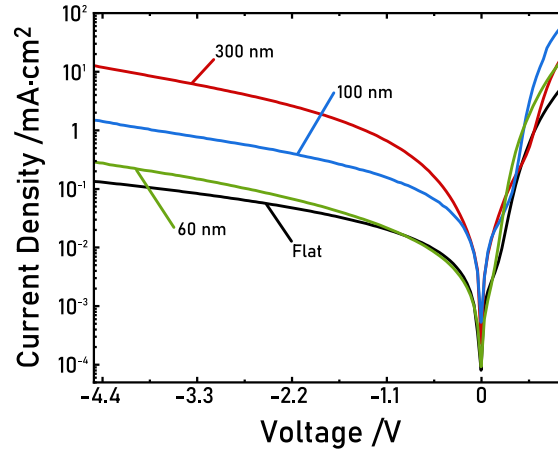


Figure 1.22: Dark Current Density plot for various nanostructuration depths and flat reference for comparison.

in collaboration with Dr. Molet. With these shallower stamps we performed a short study to check the dark currents at different nanostructure feature depth (300 nm, 100 nm and 60 nm), and we saw that for shallow nanostructures, the optical response did not change significantly, while the dark current was dramatically decreased down to the same dark current levels as the flat equivalent photodetectors (figure 1.22). We decided to keep using the shallower 60 nm nanostructure to further develop our photodetectors, since it provided good electrical and optical properties.

Parallely, we decided to study the thickness of the hole transport layer. In theory a thicker transport layer should be able to more conformally cover the nanostructured active layer surface, since a thicker layer has higher chances of completely covering the pillar walls. However, as we can see on figure 1.23 (left), the EQE of our flat photodetector is decreased with the

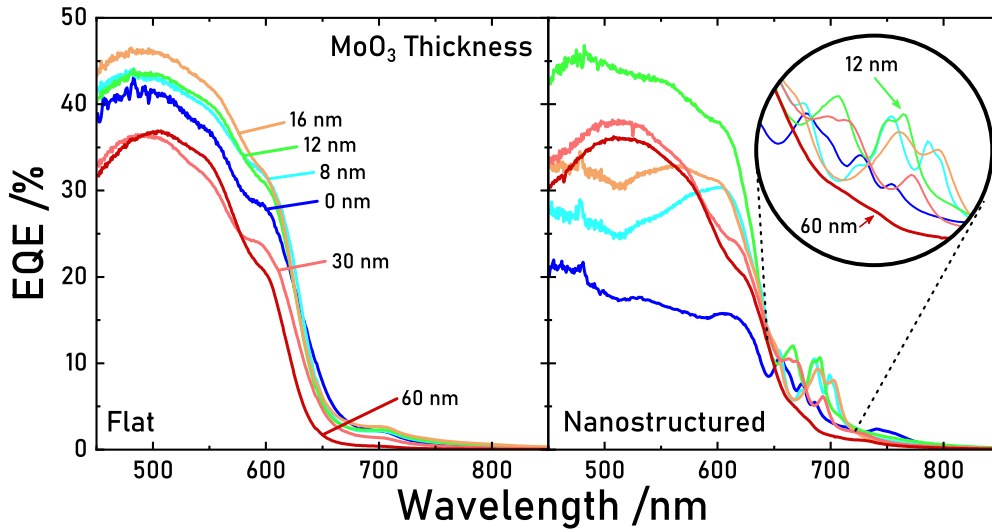


Figure 1.23: EQE curves for P3HT:PC61BM photodetectors with various MoO₃ (HTL) thicknesses for flat photodetectors, on the left, as well as nanostructured photodetectors, on the right, with a zoomed region.

thickest HTL layers. The fact that the overall electrical response of the device is hindered makes intuitive sense, since we are adding a thick poorly conducting layer between the photoactive material and the electrode. Undoubtedly, this layer is selecting the charges, but its low electrical conductivity is also lowering the charge extraction efficiency.

On the other hand, figure 1.23 shows that the EQE enhancement peaks are significantly smaller for the 30 nm MoO₃, and they completely disappear on the thickest 60 nm HTL layer. We can attribute this to a hindered optical performance, for thicker HTL layers. This is because the deposition process, although anisotropic in nature, tends to smooth out topographic features, that is why depositing a thick HTL will leave a smoother surface for the back electrode. This smoother surface leads to a less defined nanostructure on the back electrode, which is directly related to a lower overall optical response. Furthermore, since the optical contrast between the active layer and the back electrode is much more pronounced than that between the active layer and the MoO₃ layer, a thicker HTL will further lower the overall optical response and electric field enhancement within the photoactive material.

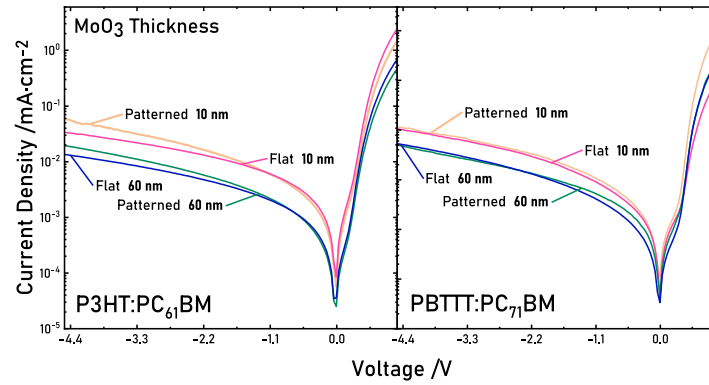


Figure 1.24: Dark Current Density plot for two different HTL thicknesses in nanostructured and flat photodetectors for both P3HT:PC₆₁BM based devices (left) and PBTTT:PC₇₁BM based devices (right).

Since the method that granted the best results for the lowering of the dark current, without greatly hindering optical performance, was the shallower nanostructuration we decided to test for pinhole formation on shallow 60 nm depth nanostructures. For that we deposited two different MoO₃ thicknesses and measured the dark current of the nanostructured and non-nanostructured devices. As we can see in figure 1.24 the difference in the dark current between nanostructured and flat devices for both 10 nm and 60 nm HTL thickness is negligible, further confirming that, at shallow feature depth the coverage is conformal. We will further confirm the complete coverage with the SEM pictures in later sections (figure 1.8), where the HTL conformally adapts to the nanostructure.

1.A.1 Active layer Thickness

Another important aspect to be studied is the active layer thickness of our photodetectors since it greatly affected the absorption capabilities and the dark currents of our devices. In this thesis, we compared a variety of active layer thicknesses to compare both their optical and electrical performance, in order to select a coarsely optimized thickness range to work with. This is by no means a full optimization process but rather an exploratory study. Furthermore, active layer thickness and dark current are also strongly correlated, since thicker layers will

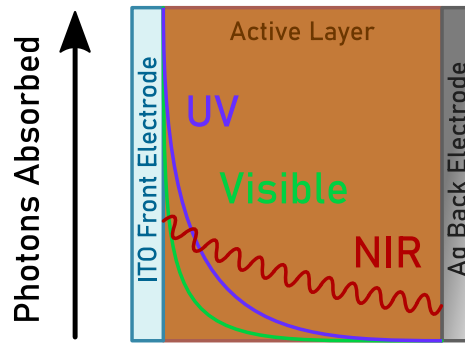


Figure 1.25: Light absorption profile across the active layer of a thick photodetector for various light wavelengths. Figure inspired by Armin et al.²

provide better rectification capabilities within the bulk hetero-junction. This correlation will also be useful to further tune and enhance the performance of our photodetectors.

In thicker layers, the majority of visible light is absorbed within the top surface of the active layer, hence most charge generation occurs there. However, since all those generated charges are far away from the back electrode, most just recombine and do not contribute to the overall current.² For NIR light however, since the absorption is much lower, photons are more evenly distributed throughout the active layer, which leads to a more homogeneous charge generation (figure 1.25). These charges are more effectively extracted since they are not highly localized on one of the electrodes. This is the phenomenon known as charge collection narrowing, and it is further described by Armin et al.²

We see that the optimal active layer thickness is not the same for different materials, mainly due to differences in charge mobility and index of refraction. Materials with higher charge mobilities will benefit from thicker active layers to absorb more light, while materials with higher refractive indices tend to couple the light more effectively.¹²⁴ By “optimal thickness”, we mean the thickness at which the subject of study, NIR range EQE enhancement, is maximized. At lower active layer thicknesses, light does not travel long enough through the active layer to

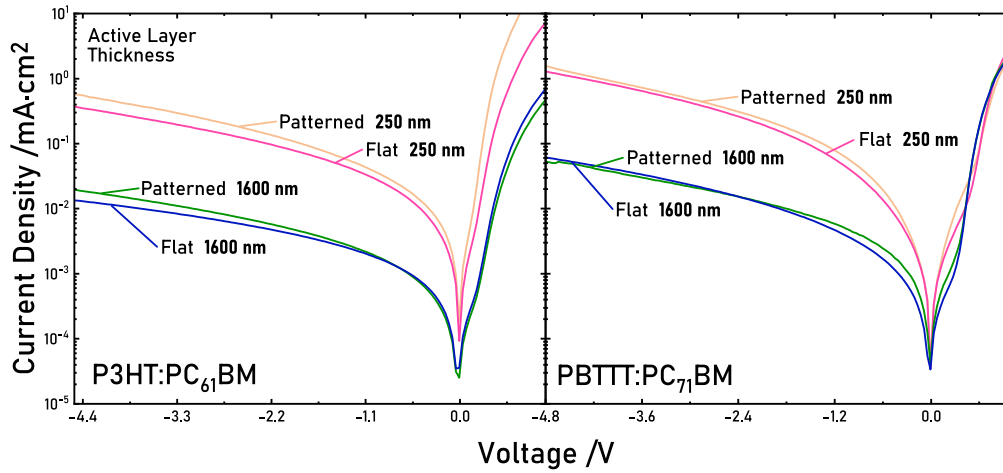


Figure 1.26: Dark Current Density plot for two different active layer thicknesses in nanostructured and flat photodetectors for both P3HT:PC₆₁BM based devices (left) and PBTTT:PC₇₁BM based devices (right).

get absorbed, while at higher thicknesses, the hindered electrical response lowers device performance, completely erasing any enhancement provided by the 2D photonic crystal. Taking this into account, our experiments have revealed a sweet spot around 700 nm for the P3HT:PC₆₁BM and 1600 nm for the PBTTT:PC₇₁BM, where device performance is maximized in the NIR region. Our hypothesis is that the optimum thickness is higher for PBTTT based active layer blends because of its higher mobility with respect to P3HT based ones.¹²⁵

We also decided to briefly assess the role of the active layer thickness on the dark current, since higher active layer thicknesses provide for better rectification capabilities. As we see in figure 1.26, thicker active layers do in fact, exhibit much lower dark currents in both P3HT:PC₆₁BM and PBTTT:PC₇₁BM based devices. This makes intuitive sense since a thick active layer will lower the overall conductivity of the device, and enhance its rectification capabilities, resulting in lower dark currents.¹¹⁹

A very interesting result from this experiment is the fact that the enhancement peak position is not significantly affected by active layer thickness (figure 1.27). While they do change in relative and absolute height, the enhanced wavelength region is strongly thickness independent. This is

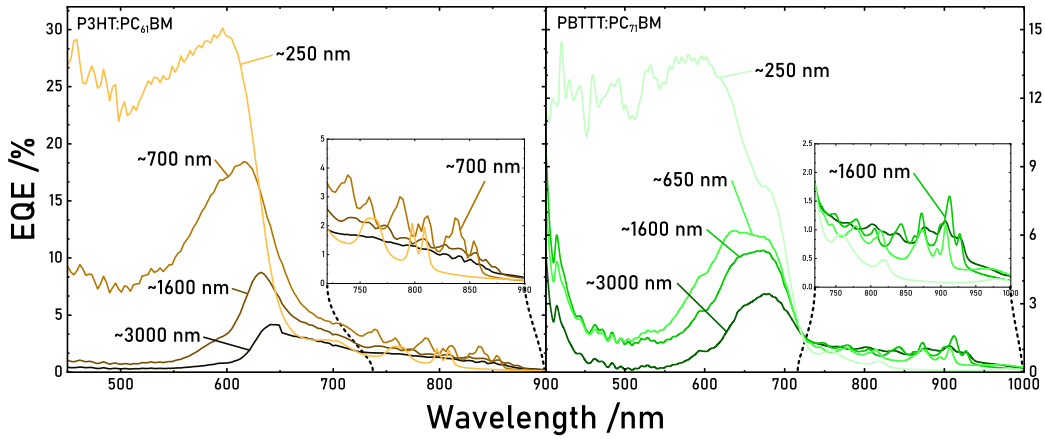


Figure 1.27: EQE response of L500 P3HT:PC₆₁BM (left) and PBTTT:PC₇₁BM (right) photodetector for different active layer thicknesses with zoomed region

more important than it might seem at first, since it means that these devices are robust against thickness variations, making them really appealing for the industry, where higher manufacturing tolerances lead to overall cost and effort reduction. This is in opposition to the cavity devices on which our devices are inspired, where thickness tolerances are extremely tight and a difference of few nanometres, completely shifts the wavelength peak.³¹

1.A.2 Annealing

To obtain the highest performing organic photodetectors we performed a brief study to assess the effects of different annealing temperatures on our device performance. Active layer annealing is usually performed, in the world of OPV, to improve device performance or stability through partial recrystallization.^{126, 127} This can be achieved in a number of different ways, but the most typical are: solvent annealing, where the material is partially redissolved in a solvent vapour to redistribute its components;^{128, 129} and thermal annealing, where the same redistribution is achieved by thermal agitation, when heating above a certain temperature, usually above the glass transition.^{4, 130, 131} In both cases what we achieve is a partial change in the crystalline properties of the active layer material, that, if done right, results in an overall improvement of our final device.

While all ETLs were thermally annealed as a part of the optimized deposition procedure, active layer annealing conditions had not been previously optimized, especially for such high thicknesses where mobility and morphology play a crucial role.^{125, 132–134}

In this work we focused on thermal annealing since it is really simple and can be applied to already encapsulated samples. Anecdotally, this method was the most interesting because, when annealing certain samples before encapsulation at high temperatures and for a long time, we could see the nanostructure pattern's iridescence slowly disappear, indicating that the diffractive features were being smoothed away. When the samples were encapsulated in epoxy resin however, since these kind of sealants are resistant to temperature, the nanostructure did not exhibit any visible change regardless of annealing time or temperature.

As we can see in figure 1.28 the performance of our devices is significantly affected by annealing the active layer. In this graph we can see that there is a certain annealing temperature range where annealed active layers greatly outperform their unannealed equivalents, where for the EQE in the NIR region the P3HT:PC61BM samples show an enhancement of around 1.8 fold while the PBTTT:PC71BM samples exhibit an impressive 8.7 fold increase. Outside of this temperature range, however, device performance can drastically drop indicating unfavourable recrystallization at higher temperatures. We attribute this performance drop to excessive recrystallization with stronger phase separation,¹³⁵ which is not desirable in most BHJ since a certain degree of well intermixed phases is necessary to enhance exciton separation.¹³⁶ Besides, the CTS is highly dependant on donor-acceptor intermixing, so phase separation can have a specially detrimental effect on its absorption strength. This results underline the importance of a correct donor-acceptor intermixing degree in CTS absorption.

We decided to anneal our devices for 20 minutes at 135°C, parameters which provided satisfactory performances for our devices. I note, however, that this was not at all an extensive study

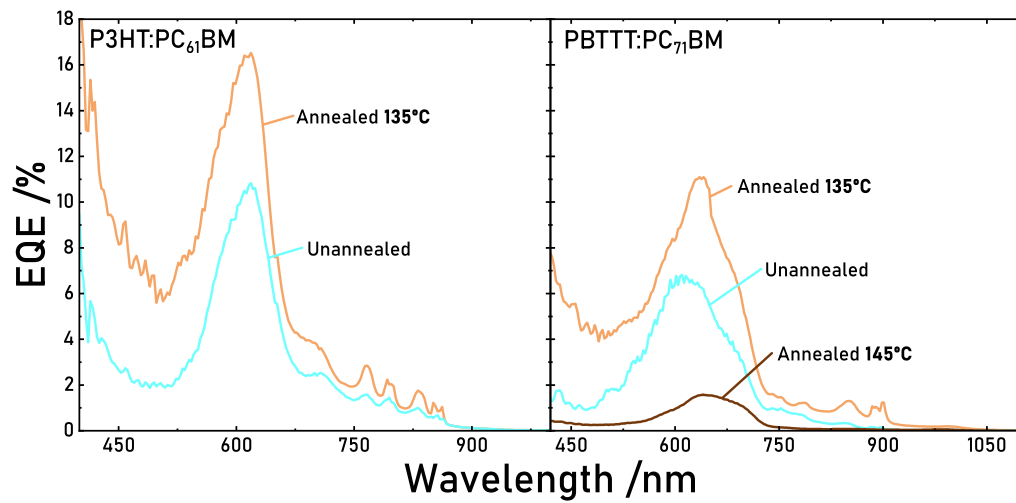


Figure 1.28: EQE response of L500 P3HT:PC₆₁BM (left) and PBTTT:PC₇₁BM (right) photodetector for different active layer annealing conditions.

and further optimization is not only possible but desirable.

Bibliography

- ¹ Martí Gibert-Roca, Pau Molet, Agustín Mihi, and Mariano Campoy-Quiles. Near infrared organic photodetectors based on enhanced charge transfer state absorption by photonic architectures. *Journal of Materials Chemistry C*, 8(28):9688–9696, 2020.
- ² Ardalan Armin, Ross D. Jansen-Van Vuuren, Nikos Kopidakis, Paul L. Burn, and Paul Meredith. Narrowband light detection via internal quantum efficiency manipulation of organic photodiodes. *Nature Communications*, 6(6343):&&&, 2015.
- ³ Sungmo Ahn, Devin Rourke, and Wounjhang Park. Plasmonic nanostructures for organic photovoltaic devices. *Journal of Optics (United Kingdom)*, 18(3):33001, 2016.
- ⁴ Gang Li, Vishal Shrotriya, Yan Yao, and Yang Yang. Investigation of annealing effects and film thickness dependence of polymer solar cells based on poly(3-hexylthiophene). *Journal of Applied Physics*, 98(4):1–6, 2005.
- ⁵ Kevin M. Coakley and Michael D. McGehee. Conjugated Polymer Photovoltaic Cells. *Chemistry of Materials*, 16(23):4533–4542, 11 2004.
- ⁶ Cephas E. Small, Sai Wing Tsang, Song Chen, Sujin Baek, Chad M. Amb, Jegadesan Subbiah, John R. Reynolds, and Franky So. Loss mechanisms in thick-film low-bandgap polymer solar cells. *Advanced Energy Materials*, 3(7):909–916, 2013.
- ⁷ Doo Hyun Ko, John R. Tumbleston, Abay Gadisa, Mukti Aryal, Yingchi Liu, Rene Lopez, and Edward T. Samulski. Light-trapping nano-structures in organic photovoltaic cells. *Journal of Materials Chemistry*, 21(41):16293–16303, 2011.

- ⁸ Binayak Dasgupta, Wei Peng Goh, Zi En Ooi, Lai Mun Wong, Chang Yun Jiang, Yi Ren, Eng Soon Tok, Jisheng Pan, Jie Zhang, and Sing Yang Chiam. Enhanced extraction rates through gap states of molybdenum oxide anode buffer. *Journal of Physical Chemistry C*, 117(18):9206–9211, 2013.
- ⁹ Gwang Hoon Jun, Sung Hwan Jin, Bin Lee, Bo Hyun Kim, Weon Sik Chae, Soon Hyung Hong, and Seokwoo Jeon. Enhanced conduction and charge-selectivity by N-doped graphene flakes in the active layer of bulk-heterojunction organic solar cells. *Energy and Environmental Science*, 6(10):3000–3006, 2013.
- ¹⁰ Leanne Murphy, Wei Hong, Hany Aziz, and Yuning Li. Organic photovoltaics with thick active layers (~ 800 nm) using a high mobility polymer donor. *Solar Energy Materials and Solar Cells*, 114:71–81, 2013.
- ¹¹ Prashant Sonar, Samarendra P. Singh, Yuning Li, Zi En Ooi, Tae Jun Ha, Ivy Wong, Mui Siang Soh, and Ananth Dodabalapur. High mobility organic thin film transistor and efficient photovoltaic devices using versatile donor-acceptor polymer semiconductor by molecular design. *Energy and Environmental Science*, 4(6):2288–2296, 2011.
- ¹² Kanwar S. Nalwa, John A. Carr, Rakesh C. Mahadevapuram, Hari K. Kodali, Sayantan Bose, Yuqing Chen, Jacob W. Petrich, Baskar Ganapathysubramanian, and Sumit Chaudhary. Enhanced charge separation in organic photovoltaic films doped with ferroelectric dipoles. *Energy and Environmental Science*, 5(5):7042–7049, 2012.
- ¹³ Bin Yang, Yongbo Yuan, Pankaj Sharma, Shashi Poddar, Rafal Korlacki, Stephen Ducharme, Alexei Gruverman, Ravi Saraf, and Jinsong Huang. Tuning the energy level offset between donor and acceptor with ferroelectric dipole layers for increased efficiency in Bilayer organic photovoltaic cells. *Advanced Materials*, 24(11):1455–1460, 2012.
- ¹⁴ Yongbo Yuan, Zhengguo Xiao, Bin Yang, and Jinsong Huang. Arising applications of ferroelectric materials in photovoltaic devices. *Journal of Materials Chemistry A*, 2(17):6027–6041, 2014.

- ¹⁵ Pavisorn Chuenchum, Pongsak Suttinon, and Piyatida Ruangrassamee. Assessment of cross-sectoral damage from water deficits under changing climate and regional development in Nan River Basin, Thailand. *World Environmental and Water Resources Congress 2017: International Perspectives, History and Heritage, Emerging Technologies, and Student Papers - Selected Papers from the World Environmental and Water Resources Congress 2017*, pages 694–709, 2017.
- ¹⁶ Peter Bermel, Chiyan Luo, Lirong Zeng, Lionel C. Kimerling, and John D. Joannopoulos. Improving thin-film crystalline silicon solar cell efficiencies with photonic crystals. *Optics Express*, 15(25):16986, 2007.
- ¹⁷ E. T. Yu and J. Van De Lagemaat. Photon management for photovoltaics. *MRS Bulletin*, 36(6):424–428, 2011.
- ¹⁸ Mikhail Parchine, Tomas Kohoutek, Maria Bardosova, and Martyn E. Pemble. Large area colloidal photonic crystals for light trapping in flexible organic photovoltaic modules applied using a roll-to-roll Langmuir-Blodgett method. *Solar Energy Materials and Solar Cells*, 185(May):158–165, 2018.
- ¹⁹ Ulrich Wilhelm Paetzold, Weiming Qiu, Friedhelm Finger, Jef Poortmans, and David Cheyns. Nanophotonic front electrodes for perovskite solar cells. *Applied Physics Letters*, 106(17), 2015.
- ²⁰ P. Peumans, V. Bulović, and S. R. Forrest. Efficient photon harvesting at high optical intensities in ultrathin organic double-heterostructure photovoltaic diodes. *Applied Physics Letters*, 76(19):2650–2652, 2000.
- ²¹ M. Niggemann, M. Glatthaar, P. Lewer, C. Müller, J. Wagner, and A. Gombert. Functional microprism substrate for organic solar cells. *Thin Solid Films*, 511-512:628–633, 2006.
- ²² Seung Bum Rim, Shanbin Zhao, Shawn R. Scully, Michael D. McGehee, and Peter Peumans. An effective light trapping configuration for thin-film solar cells. *Applied Physics Letters*, 91(24):10–13, 2007.

- ²³ Kristofer Tvingstedt, Viktor Andersson, Fengling Zhang, and Olle Inganäs. Folded reflective tandem polymer solar cell doubles efficiency. *Applied Physics Letters*, 91(12):89–92, 2007.
- ²⁴ Brendan O’Connor, Denis Nothorn, Kevin P. Pipe, and Max Shtein. High-efficiency broadband solar cell architectures based on arrays of volumetrically distributed narrowband photovoltaic fibers. *Optics Express*, 18(S3):A432, 2010.
- ²⁵ Jiwen Liu, Manoj A.G. Namboothiry, and David L. Carroll. Optical geometries for fiber-based organic photovoltaics. *Applied Physics Letters*, 90(13):1–4, 2007.
- ²⁶ Kristofer Tvingstedt, Simone Dal Zilio, Olle Inganäs, and Massimo Tormen. Trapping light with micro lenses in thin film organic photovoltaic cells. *Optics Express*, 16(26):21608, 2008.
- ²⁷ Simone Dal Zilio, Kristofer Tvingstedt, Olle Inganäs, and Massimo Tormen. Fabrication of a light trapping system for organic solar cells. *Microelectronic Engineering*, 86(4-6):1150–1154, 2009.
- ²⁸ E. Yablonovitch and G.D. Cody. Intensity enhancement in textured optical sheets for solar cells. *IEEE Transactions on Electron Devices*, 29(2):300–305, 2 1982.
- ²⁹ Patrick Campbell and Martin A. Green. The Limiting Efficiency of Silicon Solar Cells under Concentrated Sunlight. *IEEE Transactions on Electron Devices*, 33(2):234–239, 1986.
- ³⁰ Hao Wu Lin, Si Wen Chiu, Li Yen Lin, Zheng Yu Hung, Yi Hong Chen, Francis Lin, and Ken Tsung Wong. Device engineering for highly efficient top-illuminated organic solar cells with microcavity structures. *Advanced Materials*, 24(17):2269–2272, 2012.
- ³¹ Zheng Tang, Zaifei Ma, Antonio Sánchez-Díaz, Sascha Ullbrich, Yuan Liu, Bernhard Siegmund, Andreas Mischok, Karl Leo, Mariano Campoy-Quiles, Weiwei Li, and Koen Vandewal. Polymer:Fullerene Bimolecular Crystals for Near-Infrared Spectroscopic Photodetectors. *Advanced Materials*, 29(33):1–8, 2017.
- ³² Jordi Martorell. A photonic nano-structuring approach to increase energy harvesting for organic photovoltaic cells. *ICTON*, C6(2):1–1, 2012.

- ³³ Silvia Colodrero, Agustín Mihi, Leif Häggman, Manuel Ocaña, Gerrit Boschloo, Anders Hagfeldt, and Hernán Míguez. Porous one-dimensional photonic crystals improve the power-conversion efficiency of dye-sensitized solar cells. *Advanced Materials*, 21(7):764–770, 2009.
- ³⁴ John R. Tumbleston, Doo Hyun Ko, Edward T. Samulski, and Rene Lopez. Electrophotonic enhancement of bulk heterojunction organic solar cells through photonic crystal photoactive layer. *Applied Physics Letters*, 94(4):2007–2010, 2009.
- ³⁵ L. Zeng, Y. Yi, C. Hong, J. Liu, N. Feng, X. Duan, L. C. Kimerling, and B. A. Alamariu. Efficiency enhancement in Si solar cells by textured photonic crystal back reflector. *Applied Physics Letters*, 89(11), 2006.
- ³⁶ Fan Yang, Ye Zhang, Yuying Hao, Yanxia Cui, Wenyan Wang, Ting Ji, Fang Shi, and Bin Wei. Visibly transparent organic photovoltaic with improved transparency and absorption based on tandem photonic crystal for greenhouse application. *Applied Optics*, 54(34):10232, 2015.
- ³⁷ Sanjay K. Ram, Derese Desta, Rita Rizzoli, Bruno P. Falcão, Emil H. Eriksen, Michele Bellettato, Bjarke R. Jeppesen, Pia B. Jensen, Caterina Summonte, Rui N. Pereira, Arne Nylandsted Larsen, and Peter Balling. Efficient light-trapping with quasi-periodic uniaxial nanowrinkles for thin-film silicon solar cells. *Nano Energy*, 35:341–349, 2017.
- ³⁸ Emiliano R. Martins, Juntao Li, Yikun Liu, Valérie Depauw, Zhanxu Chen, Jianying Zhou, and Thomas F. Krauss. Deterministic quasi-random nanostructures for photon control. *Nature Communications*, 4:1–7, 2013.
- ³⁹ Chen Xie, Thomas Heumüller, Wolfgang Gruber, Xiaofeng Tang, Andrej Classen, Isabel Schultes, Matthew Bidwell, Andreas Späth, Rainer H. Fink, Tobias Unruh, Iain McCulloch, Ning Li, and Christoph J. Brabec. Overcoming efficiency and stability limits in water-processing nanoparticulate organic photovoltaics by minimizing microstructure defects. *Nature Communications*, 9(1):1–11, 2018.

- ⁴⁰ Emmanuel Stratakis and Emmanuel Kymakis. Nanoparticle-based plasmonic organic photovoltaic devices, 2013.
- ⁴¹ Anthony J. Morfa, Kathy L. Rowlen, Thomas H. Reilly, Manuel J. Romero, and Jao Van De Lagemaat. Plasmon-enhanced solar energy conversion in organic bulk heterojunction photovoltaics. *Applied Physics Letters*, 92(1):4–7, 2008.
- ⁴² Qiaoqiang Gan, Filbert J. Bartoli, and Zakya H. Kafafi. Plasmonic-enhanced organic photovoltaics: Breaking the 10% efficiency barrier. *Advanced Materials*, 25(17):2385–2396, 2013.
- ⁴³ Zongfu Yu, Aaswath Raman, and Shanhui Fan. Fundamental limit of light trapping in grating structures. *OPTICS EXPRESS*, 18(S3):A366–A380, 2010.
- ⁴⁴ Zongfu Yu, Aaswath Raman, and Shanhui Fan. Fundamental limit of nanophotonic light trapping in solar cells. *Proceedings of the National Academy of Sciences of the United States of America*, 107(41):17491–17496, 10 2010.
- ⁴⁵ Yongbing Long. Improving optical performance of inverted organic solar cells by microcavity effect. *Applied Physics Letters*, 95(19):4–7, 2009.
- ⁴⁶ Wilfried Vervisch, St´ephane Biondo, Guillaume Rivère, David Duch´, Ludovic Escoubas, Philippe Torchio, Jean Jacques Simon, and Judikal Le Rouzo. Optical-electrical simulation of organic solar cells: Excitonic modeling parameter influence on electrical characteristics. *Applied Physics Letters*, 98(25):0–3, 2011.
- ⁴⁷ Doo-Hyun Ko, John R. Tumbleston, Lei Zhang, Stuart Williams, Joseph M. DeSimone, Rene Lopez, and Edward T. Samulski. Photonic Crystal Geometry for Organic Polymer:Fullerene Standard and Inverted Solar Cells. *Nano Letters*, 9(7):2742–2746, 7 2009.
- ⁴⁸ Doo-hyun Ko, John R Tumbleston, Lei Zhang, Stuart Williams, Joseph M. DeSimone, Rene Lopez, and Edward T Samulski. Photonic Crystal Geometry for Organic Solar Cells. *Nano Letters*, 9(7):2742–2746, 7 2009.

- ⁴⁹ Suzushi Nishimura, Neal Abrams, Bradley A Lewis, Lara I Halaoui, Thomas E Mallouk, Kurt D Benkstein, Jao Van de Lagemaat, and Arthur J Frank. Standing wave enhancement of red absorbance and photocurrent in dye-sensitized titanium dioxide photoelectrodes coupled to photonic crystals. *Journal of the American Chemical Society*, 125(20):6306–6310, 2003.
- ⁵⁰ Isabelle Rodriguez, Fernando Ramiro-Manzano, Pedro Atienzar, Jose Manuel Martinez, Francisco Meseguer, Hermenegildo Garcia, and Avelino Corma. Solar energy harvesting in photoelectrochemical solar cells. *Journal of Materials Chemistry*, 17(30):3205–3209, 2007.
- ⁵¹ Stefan Guldin, Sven Hüttner, Matthias Kolle, Mark E Welland, Peter Müller-Buschbaum, Richard H Friend, Ullrich Steiner, and Nicolas Tétreault. Dye-sensitized solar cell based on a three-dimensional photonic crystal. *Nano Letters*, 10(7):2303–2309, 7 2010.
- ⁵² Liguojin, Jin Zhai, Liping Heng, Tianxin Wei, Liping Wen, Lei Jiang, Xiaoxu Zhao, and Xianyou Zhang. Bio-inspired multi-scale structures in dye-sensitized solar cell. *Journal of Photochemistry and Photobiology C: Photochemistry Reviews*, 10(4):149–158, 2009.
- ⁵³ Calum McDonald, Chengsheng Ni, Paul Maguire, Paul Connor, John T.S. Irvine, Davide Mariotti, and Vladimir Svrcek. Nanostructured perovskite solar cells. *Nanomaterials*, 9(10), 2019.
- ⁵⁴ James G Mutitu, Shouyuan Shi, Caihua Chen, Timothy Creazzo, Allen Barnett, Christiana Honsberg, and Dennis W Prather. Thin film solar cell design based on photonic crystal and diffractive grating structures. *Optics Express*, 16(19):15238, 2008.
- ⁵⁵ Yeonsang Park, Emmanuel Drouard, Ounsi El Daif, Xavier Letartre, Pierre Viktorovitch, Alain Fave, Anne Kaminski, Mustapha Lemit, and Christian Seassal. Absorption enhancement using photonic crystals for silicon thin film solar cells. *Optics Express*, 17(16):14312, 2009.

- ⁵⁶ Roar R. Søndergaard, Markus Hösel, and Frederik C. Krebs. Roll-to-Roll fabrication of large area functional organic materials. *Journal of Polymer Science, Part B: Polymer Physics*, 51(1):16–34, 2013.
- ⁵⁷ Christoph Brabec (Linz) and Erlangen Hauch (Erlangen). United States, 2009.
- ⁵⁸ Sichao Tong, Jun Yuan, Chujun Zhang, Chunhua Wang, Baoxing Liu, Jianqiang Shen, Huayan Xia, Yingping Zou, Haipeng Xie, Jia Sun, Si Xiao, Jun He, Yongli Gao, and Junliang Yang. Large-scale roll-to-roll printed, flexible and stable organic bulk heterojunction photodetector. *npj Flexible Electronics*, 2(1):1–8, 2018.
- ⁵⁹ Tomoyuki Yokota, Peter Zalar, Martin Kaltenbrunner, Hiroaki Jinno, Naoji Matsuhisa, Hiroki Kitanosako, Yutaro Tachibana, Wakako Yukita, Mari Koizumi, and Takao Someya. Ultraflexible organic photonic skin. *Science Advances*, 2(4):1–9, 2016.
- ⁶⁰ Riccardo Po, Gabriele Bianchi, Chiara Carbonera, and Andrea Pellegrino. "all that glisters is not gold": An analysis of the synthetic complexity of efficient polymer donors for polymer solar cells. *Macromolecules*, 48(3):453–461, 2015.
- ⁶¹ Minh Trung Dang, Lionel Hirsch, and Guillaume Wantz. P3HT:PCBM, best seller in polymer photovoltaic research. *Advanced Materials*, 23(31):3597–3602, 2011.
- ⁶² Eng Liang Lim, Chi Chin Yap, Mohd Asri Mat Teridi, Chin Hoong Teh, Abd Rashid Bin Mohd Yusoff, and Mohammad Hafizuddin Hj Jumali. A review of recent plasmonic nanoparticles incorporated P3HT: PCBM organic thin film solar cells. *Organic Electronics*, 36:12–28, 2016.
- ⁶³ Carl Poelking, Kostas Daoulas, Alessandro Troisi, and Denis Andrienko. Morphology and charge transport in P3HT: A theorist's perspective. *Advances in Polymer Science*, 265(July):139–180, 2014.

- ⁶⁴ A. Foertig, J. Rauh, V. Dyakonov, and C. Deibel. Shockley equation parameters of P3HT:PCBM solar cells determined by transient techniques. *Physical Review B - Condensed Matter and Materials Physics*, 86(11):1–7, 2012.
- ⁶⁵ Alberto Jiménez[U+2010]Solano, José[U+2010]Maria Delgado[U+2010]Sánchez, Mauricio E. Calvo, José M. Miranda[U+2010]Muñoz, Gabriel Lozano, Diego Sancho, Emilio Sánchez[U+2010]Cortezón, and Hernán Míguez. Design and realization of transparent solar modules based on luminescent solar concentrators integrating nanostructured photonic crystals. *Progress in Photovoltaics: Research and Applications*, 23(12):1785–1792, 12 2015.
- ⁶⁶ R. Santbergen and R. J.C. van Zolingen. The absorption factor of crystalline silicon PV cells: A numerical and experimental study. *Solar Energy Materials and Solar Cells*, 92(4):432–444, 2008.
- ⁶⁷ Grace Rajan, Krishna Aryal, Tasnuva Ashrafee, Shankar Karki, Abdel Rahman Ibdah, Vikash Ranjan, Robert W. Collins, and Sylvain Marsillac. Optimization of anti-reflective coatings for CIGS solar cells via real time spectroscopic ellipsometry. *2015 IEEE 42nd Photovoltaic Specialist Conference, PVSC 2015*, (1):4–7, 2015.
- ⁶⁸ Yin-Jung Chang. Suppressing lossy-film-induced angular mismatches between reflectance and transmittance extrema: optimum optical designs of interlayers and AR coating for maximum transmittance into active layers of CIGS solar cells. *Optics Express*, 22(S1):A167, 2014.
- ⁶⁹ A. Shah, J. Meier, A. Buechel, U. Kroll, J. Steinhauser, F. Meillaud, H. Schade, and D. Dominé. Towards very low-cost mass production of thin-film silicon photovoltaic (PV) solar modules on glass. *Thin Solid Films*, 502(1-2):292–299, 2006.
- ⁷⁰ Ken Zweibel. Issues in thin film PV manufacturing cost reduction. *Solar Energy Materials and Solar Cells*, 59(1):1–18, 1999.

- ⁷¹ Wenchao Zhao, Shaoqing Zhang, and Jianhui Hou. Realizing 11.3% efficiency in fullerene-free polymer solar cells by device optimization. *Science China Chemistry*, 59(12):1574–1582, 2016.
- ⁷² Boyuan Qi and Jizheng Wang. Fill factor in organic solar cells. *Physical Chemistry Chemical Physics*, 15(23):8972–8982, 2013.
- ⁷³ Sara Marina, Alberto D. Scaccabarozzi, Edgar Gutierrez-Fernandez, Eduardo Solano, Aditi Khirbat, Laura Ciammaruchi, Amaia Iturrospe, Alex Balzer, Liyang Yu, Elena Gabirondo, Xavier Monnier, Haritz Sardon, Thomas D. Anthopoulos, Mario Caironi, Mariano Campoy-Quiles, Christian Müller, Daniele Cangialosi, Natalie Stingelin, and Jaime Martin. Polymorphism in Non-Fullerene Acceptors Based on Indacenodithienothiophene. *Advanced Functional Materials*, 31(29), 2021.
- ⁷⁴ Shaoqing Zhang, Long Ye, Hao Zhang, and Jianhui Hou. Green-solvent-processable organic solar cells. *Materials Today*, 19(9):533–543, 2016.
- ⁷⁵ Xiong Gong, Minghong Tong, Yangjun Xia, Wanzhu Cai, Ji Sun Moon, Yong Cao, Gang Yu, Chan Long Shieh, Boo Nilsson, and Alan J. Heeger. High-detectivity polymer photodetectors with spectral response from 300 nm to 1450 nm. *Science*, 325(5948):1665–1667, 2009.
- ⁷⁶ Huan Wang and Dong Ha Kim. Perovskite-based photodetectors: Materials and devices. *Chemical Society Reviews*, 46(17):5204–5236, 2017.
- ⁷⁷ Robert J Bruening. Spectral irradiance scales based on filtered absolute silicon photodetectors. *Appl. Opt.*, 26(6):1051–1057, 3 1987.
- ⁷⁸ L Randall Canfield, Robert E Vest, Thomas N Woods, and Raj S Korde. Silicon photodiodes with integrated thin-film filters for selective bandpasses in the extreme ultraviolet. In *Proc.SPIE*, volume 2282, 9 1994.

- ⁷⁹Yongfang Li. Molecular design of photovoltaic materials for polymer solar cells: Toward suitable electronic energy levels and broad absorption. *Accounts of Chemical Research*, 45(5):723–733, 2012.
- ⁸⁰M. R. Antognazza, U. Scherf, P. Monti, and G. Lanzani. Organic-based tristimuli colorimeter. *Applied Physics Letters*, 90(16):21–24, 2007.
- ⁸¹Noah Strobel, Nikolaos Droseros, Wolfgang Köntges, Mervin Seiberlich, Manuel Pietsch, Stefan Schliske, Felix Lindheimer, Rasmus R. Schröder, Uli Lemmer, Martin Pfannmöller, Natalie Banerji, and Gerardo Hernandez-Sosa. Color-Selective Printed Organic Photodiodes for Filterless Multichannel Visible Light Communication. *Advanced Materials*, 32(12):&&&, 2020.
- ⁸²Dong Meng, Ran Zheng, Yepin Zhao, Elizabeth Zhang, Letian Dou, and Yang Yang. Near[U+2010]Infrared Materials: The Turning Point of Organic Photovoltaics. *Advanced Materials*, page 2107330, 2022.
- ⁸³Letian Dou, Yongsheng Liu, Ziruo Hong, Gang Li, and Yang Yang. Low-Bandgap Near-IR Conjugated Polymers/Molecules for Organic Electronics. *Chemical Reviews*, 115(23):12633–12665, 2015.
- ⁸⁴Xiaodong Liu, Yiwei Lin, Yingjie Liao, Jiazun Wu, and Yonghao Zheng. Recent advances in organic near-infrared photodiodes. *Journal of Materials Chemistry C*, 6(14):3499–3513, 2018.
- ⁸⁵Boming Xie, Zhongxin Chen, Lei Ying, Fei Huang, and Yong Cao. Near[U+2010]infrared organic photoelectric materials for light[U+2010]harvesting systems: Organic photovoltaics and organic photodiodes. *InfoMat*, 2(1):57–91, 2020.
- ⁸⁶Corsin Battaglia, Ching Mei Hsu, Karin Söderström, Jordi Escarré, Franz Josef Haug, Mathieu Charrière, Mathieu Boccard, Matthieu Despeisse, Duncan T.L. Alexander, Marco Cantoni, Yi Cui, and Christophe Ballif. Light trapping in solar cells: Can periodic beat random? *ACS Nano*, 6(3):2790–2797, 2012.

- ⁸⁷ Gerasimos Konstantatos and Edward H. Sargent. Nanostructured materials for photon detection. *Nature Nanotechnology*, 5(6):391–400, 2010.
- ⁸⁸ Carsten Deibe, Thomas Strope, and Vladimir Dyakonov. Role of the charge transfer state in organic donor-acceptor solar cells. *Advanced Materials*, 22(37):4097–4111, 2010.
- ⁸⁹ Priyadarshi Panda, Dirk Veldman, Jörgen Sweelssen, Jolanda J.A.M. Bastiaansen, Bea M.W. Langeveld-Voss, and Stefan C.J. Meskers. Charge transfer absorption for π -conjugated polymers and oligomers mixed with electron acceptors. *Journal of Physical Chemistry B*, 111(19):5076–5081, 2007.
- ⁹⁰ Eric T. Hoke, Koen Vandewal, Jonathan A. Bartelt, William R. Mateker, Jessica D. Douglas, Rodrigo Noriega, Kenneth R. Graham, Jean M J Fréchet, Alberto Salleo, and Michael D. McGehee. Recombination in polymer:Fullerene solar cells with open-circuit voltages approaching and exceeding 1.0 V. *Advanced Energy Materials*, 3(2):220–230, 2013.
- ⁹¹ Tsz Wai Ng, Ming Fai Lo, Man Keung Fung, Wen Jun Zhang, and Chun Sing Lee. Charge-transfer complexes and their role in exciplex emission and near-infrared photovoltaics. *Advanced Materials*, 26(31):5569–5574, 2014.
- ⁹² Kyohei Nakano, Kaori Suzuki, Yujiao Chen, and Keisuke Tajima. Roles of Energy/Charge Cascades and Intermixed Layers at Donor/Acceptor Interfaces in Organic Solar Cells. *Scientific Reports*, 6(July):1–11, 2016.
- ⁹³ Chia Ming Yang, Pei Yu Tsai, Sheng Fu Horng, Kuan Chen Lee, Shin Rong Tzeng, Hsin Fei Meng, Jow Tsong Shy, and Ching Fong Shu. Infrared photocurrent response of charge-transfer exciton in polymer bulk heterojunction. *Applied Physics Letters*, 92(8):7–10, 2008.
- ⁹⁴ Hamidreza Chalabi, David Schoen, and Mark L. Brongersma. Hot-electron photodetection with a plasmonic nanostripe antenna. *Nano Letters*, 14(3):1374–1380, 2014.
- ⁹⁵ Shumu Li, Dingjiang Xue, Wei Xu, Yongqiang Feng, Jingxia Wang, Guoqiang Zhang, Xi-angyue Meng, Chunru Wang, Yanlin Song, and Chunying Shu. Improving the photo current

- of the [60]PCBM/P3HT photodetector device by using wavelength-matched photonic crystals. *Journal of Materials Chemistry C*, 2(8):1500–1504, 2014.
- ⁹⁶ A. G. MacEdo, F. Zanetti, A. Mikowski, J. C. Hummelen, C. M. Lepienski, M. G.E. Da Luz, and L. S. Roman. Improving light harvesting in polymer photodetector devices through nanoindented metal mask films. *Journal of Applied Physics*, 104(3):&&&, 2008.
- ⁹⁷ E. Yablonovitch. Photonic crystals. *Journal of Modern Optics*, 41:173–194, 1994.
- ⁹⁸ Se Woong Baek, Pau Molet, Min Jae Choi, Margherita Biondi, Olivier Ouellette, James Fan, Sjoerd Hoogland, F. Pelayo García de Arquer, Agustín Mihi, and Edward H. Sargent. Nanostructured Back Reflectors for Efficient Colloidal Quantum-Dot Infrared Optoelectronics. *Advanced Materials*, 31(33):1901745, 2019.
- ⁹⁹ Ping Shen, Guoxin Wang, Bonan Kang, Wenbin Guo, and Liang Shen. High-Efficiency and High-Color-Rendering-Index Semitransparent Polymer Solar Cells Induced by Photonic Crystals and Surface Plasmon Resonance. *ACS Applied Materials and Interfaces*, 10:6513–6520, 2018.
- ¹⁰⁰ Lin Xu, Cyril Aumaitre, Yann Kervella, Gérard Lapertot, Cristina Rodríguez-Seco, Emilio Palomares, Renaud Demadrille, and Peter Reiss. Increasing the Efficiency of Organic Dye-Sensitized Solar Cells over 10.3% Using Locally Ordered Inverse Opal Nanostructures in the Photoelectrode. *Advanced Functional Materials*, 28(15):1706291, 2018.
- ¹⁰¹ Marina Mariano, Gregory Kozyreff, Luis G. Gerling, Pablo Romero-Gomez, Joaquim Puigdollers, Jorge Bravo-Abad, and Jordi Martorell. Intermittent chaos for ergodic light trapping in a photonic fiber plate. *Light: Science and Applications*, 5:e16216–e16216, 2016.
- ¹⁰² Younan Xia and George M. Whitesides. Soft Lithography. *Angewandte Chemie International Edition*, 37(5):550–575, 3 1998.

- ¹⁰³ F. Pelayo García De Arquer, Ardalan Armin, Paul Meredith, and Edward H. Sargent. Solution-processed semiconductors for next-generation photodetectors. *Nature Reviews Materials*, 2017.
- ¹⁰⁴ Zhi Hao Chen, Peng Qing Bi, Xiao Yu Yang, Meng Si Niu, Kang Ning Zhang, Lin Feng, and Xiao Tao Hao. Quantitatively Characterized Crystallization Effect on Recombination Energy Loss in Non-Fullerene Organic Solar Cells. *Journal of Physical Chemistry C*, 123(20):12676–12683, 2019.
- ¹⁰⁵ Nidhi Sharma, Saral K. Gupta, and Chandra Mohan Singh Negi. Influence of active layer thickness on photovoltaic performance of PTB7:PC70BM bulk heterojunction solar cell. *Superlattices and Microstructures*, 135(August):106278, 2019.
- ¹⁰⁶ Austin L. Jones, Carr Hoi Yi Ho, Parand R. Riley, Indunil Angunawela, Harald Ade, Franky So, and John R. Reynolds. Investigating the active layer thickness dependence of non-fullerene organic solar cells based on PM7 derivatives. *Journal of Materials Chemistry C*, 8(43):15459–15469, 2020.
- ¹⁰⁷ Younan Xia, John A Rogers, Kateri E Paul, and George M Whitesides. Unconventional Methods for Fabricating and Patterning Nanostructures. *Chem. Rev*, 99(7):1823–1848, 1999.
- ¹⁰⁸ Panagiotis E. Keivanidis, Peter K.H. Ho, Richard H. Friend, and Neil C. Greenham. The dependence of device dark current on the active-layer morphology of solution-processed organic photodetectors. *Advanced Functional Materials*, 20(22):3895–3903, 2010.
- ¹⁰⁹ Biswajit Ray, Pradeep R. Nair, and Muhammad A. Alam. Annealing dependent performance of organic bulk-heterojunction solar cells: A theoretical perspective. *Solar Energy Materials and Solar Cells*, 95(12):3287–3294, 2011.
- ¹¹⁰ You Wu, Xiao Juan Sun, Yu Ping Jia, and Da Bing Li. Review of improved spectral response of ultraviolet photodetectors by surface plasmon. *Chinese Physics B*, 27(12), 2018.

- ¹¹¹ R F Potter and W L Eisenman. Infrared Photodetectors: A Review of Operational Detectors. *Applied Optics*, 1(5):567, 1962.
- ¹¹² Vincenzo Pecunia. Efficiency and spectral performance of narrowband organic and perovskite photodetectors: A cross-sectional review, 2019.
- ¹¹³ Yan Yao, Yongye Liang, Vishal Shrotriya, Shengqiang Xiao, Luping Yu, and Yang Yang. Plastic near-infrared photodetectors utilizing low band gap polymer. *Advanced Materials*, 19(22):3979–3983, 2007.
- ¹¹⁴ A. H. Fallahpour, S. Kienitz, and P. Lugli. Origin of Dark Current and Detailed Description of Organic Photodiode Operation under Different Illumination Intensities. *IEEE Transactions on Electron Devices*, 64(6):2649–2654, 2017.
- ¹¹⁵ William T. Hammond and Jiangeng Xue. Organic heterojunction photodiodes exhibiting low voltage, imaging-speed photocurrent gain. *Applied Physics Letters*, 97(7):1–4, 2010.
- ¹¹⁶ Jae Un Ha, Kyoungwhan Kim, Seongwon Yoon, Kyu Min Sim, Jangwhan Cho, and Dae Sung Chung. Synergetic Effect of a Surfactant on the Facile Fabrication and High Detectivity of an Inverted Organic Bulk Heterojunction Photodiode. *ACS Photonics*, 4(8):2085–2090, 2017.
- ¹¹⁷ Hanyu Wang, Shen Xing, Yifan Zheng, Jaemin Kong, Junsheng Yu, and André D. Taylor. Three-Phase Morphology Evolution in Sequentially Solution-Processed Polymer Photodetector: Toward Low Dark Current and High Photodetectivity. *ACS Applied Materials and Interfaces*, 10(4):3856–3864, 2018.
- ¹¹⁸ E. S. Zaus, S. Tedde, J. Fürst, D. Henseler, and G. H. Döhler. Dynamic and steady state current response to light excitation of multilayered organic photodiodes. *Journal of Applied Physics*, 101(4), 2007.
- ¹¹⁹ Giulio Simone, Matthew J. Dyson, Stefan C.J. Meskers, René A.J. Janssen, and Gerwin H. Gelinck. Organic Photodetectors and their Application in Large Area and Flexible Image Sensors: The Role of Dark Current. *Advanced Functional Materials*, 30(20), 2020.

- ¹²⁰ Hugh L. Zhu, Wallace C.H. Choy, Wei E.I. Sha, and Xingang Ren. Photovoltaic Mode Ultraviolet Organic Photodetectors with High On/Off Ratio and Fast Response. *Advanced Optical Materials*, 2(11):1082–1089, 2014.
- ¹²¹ Matthias Jahnel, Michael Thomschke, Sascha Ullbrich, Karsten Fehse, Jong Deok An, Hoon Park, Karl Leo, Chan Im, and Volker Kirchhoff. On/off-ratio dependence of bulk hetero junction photodiodes and its impact on electro-optical properties. *Microelectronic Engineering*, 152:20–25, 2016.
- ¹²² Francesco Arca, Sandro F. Tedde, Maria Sramek, Julia Rauh, Paolo Lugli, and Oliver Hayden. Interface trap states in organic photodiodes. *Scientific Reports*, 3, 2013.
- ¹²³ Cristiano Matricardi, Juan Luis Garcia-Pomar, Pau Molet, Luis Alberto Pérez, Maria Isabel Alonso, Mariano Campoy-Quiles, and Agustín Mihi. High-Throughput Nanofabrication of Metasurfaces with Polarization-Dependent Response. *Advanced Optical Materials*, 8(20):1–8, 2020.
- ¹²⁴ Laura Stevens, Oliver Höhn, Mario Hanser, Nico Tucher, Claas Müller, Stefan Glunz, and Benedikt Bläsi. Impact of the refractive index on coupling structures for silicon solar cells. *Journal of Photonics for Energy*, 11(02):1–14, 2021.
- ¹²⁵ Iain McCulloch, Martin Heeney, Clare Bailey, Kristijonas Genevicius, Iain MacDonald, Maxim Shkunov, David Sparrowe, Steve Tierney, Robert Wagner, Weimin Zhang, Michael L. Chabinyc, R. Joseph Kline, Michael D. McGehee, and Michael F. Toney. Liquid-crystalline semiconducting polymers with high charge-carrier mobility. *Nature Materials*, 5(4):328–333, 2006.
- ¹²⁶ Marisol Reyes-Reyes, Kyungkon Kim, James Dewald, Román López-Sandoval, Aditya Avadhanula, Seamus Curran, and David L Carroll. Meso-structure formation for enhanced organic photovoltaic cells. *Organic Letters*, 7(26):5749–5752, 2005.

- ¹²⁷ Kyungkon Kim, Jiwen Liu, Manoj A.G. Namboothiry, and David L Carroll. Roles of donor and acceptor nanodomains in 6% efficient thermally annealed polymer photovoltaics. *Applied Physics Letters*, 90(16):1–4, 2007.
- ¹²⁸ Kuan Sun, Zeyun Xiao, Eric Hanssen, Michael F.G. Klein, Henk H. Dam, Marina Pfaff, Dagmar Gerthsen, Wallace W.H. Wong, and David J Jones. The role of solvent vapor annealing in highly efficient air-processed small molecule solar cells. *Journal of Materials Chemistry A*, 2(24):9048–9054, 2014.
- ¹²⁹ Said Karim Shah, Jahangeer Khan, Irfan Ullah, and Yaqoob Khan. Optimization of active-layer thickness, top electrode and annealing temperature for polymeric solar cells. *AIMS Materials Science*, 4(3):789–799, 2017.
- ¹³⁰ Marisol Reyes-Reyes, Kyungkon Kim, and David L Carroll. High-efficiency photovoltaic devices based on annealed poly(3-hexylthiophene) and 1-(3-methoxycarbonyl)-propyl-1-phenyl- (6,6) C61 blends. *Applied Physics Letters*, 87(8), 2005.
- ¹³¹ Koji Yazawa, Yoshio Inoue, Takakazu Yamamoto, and Naoki Asakawa. Twist glass transition in regioregulated poly(3-alkylthiophene). *Physical Review B - Condensed Matter and Materials Physics*, 74(9):1–12, 2006.
- ¹³² Ishan C. Ghosekar and Ganesh C. Patil. Impact of concentration variation and thermal annealing on performance of multilayer OSC consisting of sandwiched P3HT layer between PEDOT:PSS and P3HT:PCBM. *Microelectronic Engineering*, 221:111195, 2020.
- ¹³³ Joydeep Munshi and Ganesh Balasubramanian. Investigating blend morphology of P3HT:PCBM bulk heterojunction solar cells by classical atomistic simulations—Progress and prospects, 2020.
- ¹³⁴ Wenluan Zhang, Hao Shen, Brett W. Guralnick, Brian J. Kirby, Ngoc A. Nguyen, Roddel Remy, Charles F. Majkrzak, and Michael E. Mackay. Correlation between morphology and device performance of pBTTT:PC71BM solar cells. *Solar Energy Materials and Solar Cells*, 155:387–396, 2016.

- ¹³⁵ Chaohong Zhang, Alexander Mumyatov, Stefan Langner, José Darío Perea, Thaer Kassar, Jie Min, Lili Ke, Haiwei Chen, Kirill L. Gerasimov, Denis V. Anokhin, Dimitri A. Ivanov, Tayebbeh Ameri, Andreas Osvet, Diana K. Susarova, Tobias Unruh, Ning Li, Pavel Troshin, and Christoph J. Brabec. Overcoming the Thermal Instability of Efficient Polymer Solar Cells by Employing Novel Fullerene-Based Acceptors. *Advanced Energy Materials*, 7(3), 2017.
- ¹³⁶ Chen Zhao, Xianfeng Qiao, Bingbing Chen, and Bin Hu. Thermal annealing effect on internal electrical polarization in organic solar cells. *Organic Electronics*, 14(9):2192–2197, 2013.